Punjab University Journal of Mathematics (2026), 58(03), 331- 385
https://doi.org/10.52280/pujm.2026.58(03)04

Impact of Vaccination on Influenza Disease Transmission in Humans and Birds: Sensitivity and Bifurcation Analysis within Fractional Framework

Received
12 January, 2026

Revised
08 July, 2026

Accepted
26 July, 2026

Published Online
17 August, 2026

*Usama Atta, Aqeel Ahmad, Sadia Sattar
Department of Mathematics,
Ghazi University, D.G. Khan, Pakistan

Abstract. Avian influenza is a zoonotic disease that spreads from birds to humans through viral infection and poses a substantial threat to the poultry industry, which can result in severe financial consequences as well as serious public health concerns for the community. To control the spread of avian influenza, effective control measures such as vaccination are important. In order to highlight the influence of the vaccine on infected humans and birds, this study formulates a novel fractal-fractional avian influenza model in the Mittag-Leffler sense. We perform comprehensive qualitative and quantitative analysis, including verification of the presence of a single solution, positivity and boundedness of solutions, influenza-free and existing equilibrium points, the threshold parameter $\mathcal{R}_0$, the local and global stability of the influenza-free equilibrium points, the presence of forward transcritical bifurcation, and the local and global sensitivity analysis. Through local and global stability of Influenza-free equilibrium points, we verify that infection in birds stops and the chances of Influenza spread decrease when $\mathcal{R}_0 < 1$, while outbreaks and human transmission are possible when $\mathcal{R}_0 > 1$. We provide statistical analysis to show the symmetric behaviour of the compartments and the chaos test to reveal the bounded nature of all compartments of the model. In order to obtain numerical solutions, we derive a numerical technique based on Newton polynomials. We provide the phase plots illustrating the interactions between the human and bird compartments. The sensitivity analysis identifies transmission rate, recruitment, vaccination, and recovery as the most influential factors in controlling avian influenza. Through the zoonotic transmission pathway, these measures not only stabilize the bird population but also provide indirect protection to the human population.

AMS (MOS) Subject Classification Codes: 34A34; 34C23; 34D20; 65L20
Key Words: Avian influenza; Bird flu; Transcritical bifurcation; Fractal-fractional; Statistical analysis; Chaos; Newton polynomial..

**Corresponding Author* : usamaatta1111@gmail.com

1. Introduction

1.1. **Introduction to the disease.** Avian influenza spreads through the influenza virus, sometimes known as bird flu. Humans may contract it from direct or indirect contact with infected birds or contaminated surfaces, although it primarily affects wild birds and poultry. Because of its high case fatality rate and mutation potential, the disease poses a major threat to public health even though human-to-human transmission is incredibly rare. After being discovered in humans for the first time in Hong Kong in 1997, H5N1 has now spread to 16 countries, causing epidemics and a high case fatality rate (50%) because of serious consequences such as pneumonia and breathing difficulties. Numerous nations in Asia, Africa, Europe, and the Middle East have reported outbreaks, with Egypt emerging as an H5N1 endemic. The virus can produce symptoms ranging from moderate respiratory problems to severe pneumonia, acute respiratory distress, and neurological consequences. It is transmitted by contact with the saliva, excrement, or respiratory droplets of infected birds. Laboratory testing of eye or respiratory swabs is usually required for diagnosis. Early antiviral therapy can lessen the severity of the illness, but prevention, which includes wearing protective gear, maintaining good hygiene, and doing surveillance, is still essential. The possibility of a genetic mutation for human-to-human transmission increases concerns about a possible pandemic, underscoring the need for ongoing research and readiness, even though the majority of recent cases, especially in the US, have been mild. After outbreaks in poultry and migratory birds in January, the first case of H5N1 Avian influenza in 2022 was the recent death of an 11-year-old in Delhi. Although they can infect humans and domestic animals, avian influenza type A viruses (identified by HA/NA surface proteins, such as H5N1 and H7N9) naturally circulate among wild birds. More than 700 human H5N1 infections in 16 countries since 1997 have resulted in a 60% fatality rate, with children and young adults being the main victims. Rare human-to-human transmission has been documented in familial clusters, and transmission happens through contact with diseased birds or polluted surfaces. Mild symptoms like fever and coughing might progress to more serious ones like pneumonia and respiratory failure. Although there is no proof of persistent aerosol transmission, experts advise poultry workers to take precautions [38]. Figure 1 shows the sources responsible for spreading Avian Influenza and the number of cases in the US [18].

1.2. **Literature review.** To understand the phenomenon of the spread and eradication of infectious diseases like avian influenza, mathematical modeling is crucial [24, 36]. It provides several methods for combining environmental, biological, and epidemiological parameters in order to investigate the spread of disease, forecast outbreak patterns, and assess the possible influence of control measures. In the case of avian influenza, which mainly affects humans, mathematical models are helpful in estimating the contribution of environmental factors, immunization, and interspecies interactions. Models can help us to identify crucial thresholds, such as the reproductive number, beyond which an epidemic may arise by simulating various cases. Furthermore, models enable public health officials to evaluate the efficacy of measures such as vaccines, quarantine, or the removal of infectious birds. Therefore, mathematical modeling is used as a theoretical tool and as a practical decision-support system to guide policymakers and reduce the spread of avian influenza.

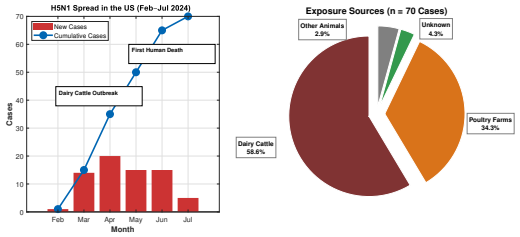

(A) Avian influenza cases in 2024 from February to July.

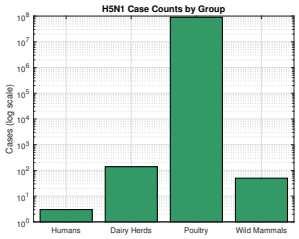

(B) The bar chart shows that poultry is the main reason for avian influenza transmission.

FIGURE 1. The plot shows the number of cases and different sources of avian influenza spread.

Compartmental models may predict spillover events from poultry to humans with 78% accuracy, when appropriately parameterized with farm-level data. Mathematical modeling helps us to better understand the non-linear effects of vaccination in poultry populations, the role of environmental persistence of viruses, and the threshold conditions for sustained human-to-human transmission. These modeling techniques have shown their usefulness in pandemic preparedness by directly influencing WHO vaccination guidelines and culling procedures during outbreaks [28].

A lot of mathematical models have been developed to understand the transmission patterns of Avian Influenza and to suggest control measures to eradicate the prevalence of Avian influenza. The fractional calculus is a more advanced approach to modeling real-world phenomena than classical integer-order calculus, especially because it is able to incorporate memory effects and hereditary properties of the systems under study. In many biological and physical systems, nonlocal behaviors and fading memory are present, which are fully captured by fractional-order models but cannot be captured by integer-order models. Fractional calculus has been thoroughly used in the modeling of epidemics in recent years for a variety of diseases including rubella [3], COVID-19 [13, 14, 21] and many other diseases. Several mathematical models have been developed to study the dynamics of avian influenza. Here, we are providing a summary of the few relevant and recent studies on avian influenza in the integer and fractional sense.

1.3. **Motivation of study.** Researchers have devised a number of definitions for fractional calculus, such as the conformable derivative, the Caputo derivative, the Caputo-Fabrizio derivative, and the Atangana-Baleanu derivative [11, 15]. These definitions do, however, have some drawbacks. The Caputo derivative is defined only for differentiable functions, has more stringent differentiability requirements, and necessitates the computation of classical derivatives in advance, whereas the conformable derivative lacks basic fractional features. When the derivative order is 1, the Caputo-Fabrizio definition, which uses a local kernel, is unable to recover the original function since its associated integral is not really fractional. When compared to other fractional operators, the Atangana-Baleanu fractional derivative frequently shows better modeling abilities for complicated events. The fractal fractional

TABLE 1. Summary of recent studies on avian influenza in integer-order sense.

Sr. No	Main contributions	Outcomes	Citation
1	Time-varying contact rate, the seasonality effect in the model including latent, infected, asymptomatic, and treated humans, the effective reproduction number; existence of unique positive solution, R-K 45 numerical method.	Periodic solutions exhibit a period-doubling bifurcation as the amplitude of seasonality increases; comparison of model outcomes with real data shows consistency.	[31]
2	Model with the impact of vaccination and treatment interventions.	A combination of vaccination and treatment reduces the prevalence of avian influenza; early and widespread vaccination, coupled with prompt treatment of infected birds, is the most effective strategy.	[33]
3	SEIAVR model solved with Range-Kutta method, reproduction number, and local and global stability.	Infection rate and exposure period are very sensitive parameters. The model result compared with the real data shows good performance.	[30]
4	Reproduction number, equilibrium points, and their stabilities.	Disease wanes and disease-free equilibrium is locally stable when $\mathcal{R}_0 < 1$; an endemic equilibrium point is stable when $\mathcal{R}_0 > 1$. The non-linear incidence reduces the influenza disease spread. Vaccination, isolation, and treatment control the disease spread.	[35]
5	Applied ANN to simulate the SVEIR PDE model with spatial diffusion, employing the Levenberg–Marquardt backpropagation approach to train the ANN; dataset generated through the finite difference technique, and performance validated through the smallest mean square error.	Regression and state transition plots illustrate the training, testing, and validation processes. Small absolute error confirms the accuracy.	[45]
6	SIR model integrating seasonality and waning immunity with the higher transmission rate in winter seasons, incorporating the decline of immunity after infection by considering multiple recovered compartments using data from Spain.	The outcomes show that the model replicates the reported data.	[9]
7	Estimated the efficacy of the vaccine using an SEIR-type model by distinguishing vaccinated and unvaccinated humans based on real data from Spain. The model incorporates the vaccine attenuation factor related to the vaccine efficacy.	The influenza vaccine has an efficacy of 76.7%, and the risk of infectiousness is five times larger for an unvaccinated person.	[4]

TABLE 2. Summary of recent studies on avian influenza in fractional-order sense.

Sr. No	Main contributions	Outcomes	Citation
8	SEIR model with treatment, local and global stability.	The treatment declines the infected, exposed, and treated humans, but susceptible humans increase.	[29]
9	Caputo fractional-order model describing within-host dynamics incorporating autophagy and immune-mediated clearance of the virus. The interplay between autophagy and adaptive immunity shows a synergistic mechanism of viral clearance.	Immune response and autophagy contribute to a marked decrease in viral load and infected cell count in the progression stage of infection. Role of intracellular and immune-mediated processes in regulating infection severity.	[34]
10	Four-dimensional influenza model using the Caputo derivative, simulated the role of fractional derivative using modified Adams-Bashforth-Moulton and Runge-Kutta methods, compares system dynamics with and without control measures.	Fractional-order dynamics influence the behavior of the model, altering system stability and trajectories.	[37]
11	The efficacy of fractional models with ABC, Caputo–Fabrizio, and Caputo derivatives is compared to the performance of integer-order models using data from Saudi Arabia, positivity, limitations, and symmetry of the numerical scheme.	The fractional-order models demonstrated superior accuracy, producing smaller error than the classical model. Thus, fractional-order models perform better than integer-order models.	[1]
12	Fractal-fractional model, using Schauder and Banach fixed point theorems, demonstrates solution existence and uniqueness, the Adams–Bashforth method.	Ulam-Hyers stability techniques ensure the model's reliability	[44]
13	Fractional-order optimal control model in the Caputo sense solved using the forward–backward sweep method with L_1 discretization, the stability of equilibria, and existence of bifurcation.	Numerical outcomes were stable and consistent with analytic predictions.	[39]
14	Caputo fractional-order model involving two viral strains with humans, poultry, and a contaminated environment, integrating awareness to modify transmission rates. Six control measures, including vaccine, treatment, culling of infected birds, environmental cleaning, and awareness.	The fractional-order alters the epidemic curve and the cost-efficiency of interventions; a combined strategy is the most effective for reducing human infections and mitigating environmental and avian sources.	[17]
15	Existence and uniqueness of fractional-order model stability; a unique endemic equilibrium exists.	Using real data, 80 percent vaccine efficacy and treatment control the disease's spread.	[6]

TABLE 3. Summary of recent studies on avian influenza in fractional-order sense.

Sr. No	Main contributions	Outcomes	Citation
16	resistant and non-resistant flu strain models in the fractal–fractional sense, the presence of solutions, stability, and numerical technique based on Lagrange's interpolation polynomial. Ulam stability.	A more realistic approach of the fractal–fractional-orders is closer to classical cases. The S, I, I_R rapidly decrease in the early days but later on get stable, while recovered humans increased first and then decreased after a few days.	[25]
17	ABC fractional derivative and fractal–fractional-order model with two distinct numerical approaches, stability.	The model is stable when the reproduction number is less than one. The fractal–fractional provides powerful results as compared to the fractional and integer-order derivative.	[8]
18	Studied the ABC fractional SEIR model and the ARIMA model to predict seasonal evolution using the real data from Saudi Arabia.	The fractional-order model performs better than the ARIMA model and agrees with real data. Increasing the natural birth rate, transmission rate, and incubation rate rises Influenza cases.	[7]
19	Piecewise stochastic fractional-order model with crossover behavior incorporating half-saturated transmission rate. The stochastic threshold number predicts extinction and persistence of pathogens.	Piecewise operator studies crossover behavior that traditional derivatives cannot.	[5]
20	ABC fractional-order system to study the influenza spread in Saudi Arabia, solved through the fractional Euler method. Stability of the equilibrium points.	The outcomes by the fractional-order system are more accurate than the integer-order model.	[2]
21	Fractional-order model to study three-strain influenza disease incorporating treatment. Four equilibrium points, including the disease-free equilibrium and endemic equilibrium, and reproduction numbers for each strain.	Fractional-order influences the rate of convergence and global stability of equilibrium points. Treatment decreases the spread of all three strains.	[43]
22	Fractional-order model with the Caputo-Fabrizio derivative including distinct contact rates between exposed and infected individuals. Existence and uniqueness of the solution, the series solution using the Laplace transform method, and the predictor-corrector method.	Contact rate with exposed humans is more crucial in disease spread. The Caputo-Fabrizio derivative provides valuable insights.	[19]

operator, which goes beyond earlier definitions, was presented by [10] to handle larger dynamic properties. By simultaneously incorporating memory effects (by fractional-order ρ) and spatial heterogeneity (via fractal dimension ζ), the fractal fractional Mittag-Leffler operator is a substantial improvement over traditional fractional operators. FFM has spatial scaling qualities that are crucial for modeling multi-scale disease dynamics, in contrast to Caputo or Riemann-Liouville derivatives, which solely handle temporal memory. Superior mathematical qualities of the Mittag-Leffler kernel allow for seamless transitions between the power-law and exponential memory regimes as well as non-singular, non-local behavior that generalizes exponential decay. As compared to other fractional and fractal-fractional differential operators, FFM provides clear benefits. Its dual-parameter structure maintains dimensional consistency while capturing both temporal memory and spatial clustering. It is non-singular and thus removes singularity problems found in the Caputo derivative. The solutions obtained by applying FFM are better, as they are more stable and converge to the exact solution. It models cross-species transmission through fractional-order dependent viral persistence and spatially heterogeneous transmission through fractal-fractional scaling for epidemiological applications. In particular, FFM performs better than pure fractal operators in memory effect representation, surpasses exponential kernels in long-term persistence modeling, and excels power-law kernels in short-term dynamics. As a result, it is the most complete operator for recording intricate dynamics of avian influenza in every compartment [40].

1.4. **Innovative contributions.** The innovative contributions addressed by this study are as follows: We have developed the $S^{\hbar}V^{\hbar}I^{\hbar}R^{\hbar}S^{b}V^{b}I^{b}R^{b}$ model to show the influence of the vaccine on infected humans and birds, incorporating the fractal-fractional operator in the Mittag-Leffler sense. The developed model is then subjected to comprehensive qualitative and quantitative analysis, including confirmation of the presence of a positive and bounded solution, local and global stability of influenza-free equilibrium points, and local and global sensitivity analysis. After this, we verify the existence of forward transcritical bifurcation at $\mathcal{R}_0 = 1$. Numerical solutions are performed through 2D contour and 3D bar plots to show the dynamics of the FFM operator using the procedure based on Newton polynomials. Furthermore, we perform the 0-1 chaos test and comprehensive statistical analysis to quantify the dynamical complexity and variability of each compartment in addition to phase plot analysis. This integrated framework provides deeper epidemiological insight than classical models and supports more reliable outbreak forecasting.

1.5. **Arrangement of study.** The remaining part of the article is organized as follows: In Section 2, we have formalized the avian influenza fractal fractional model in the Mittag-Leffler sense. Section 3 studies the fundamental properties of the model, such as the existence of a positive, bounded solution; equilibrium points and their stability; reproductive number; local and global sensitivity analysis; chaos test; statistical analysis and phase plots of the suggested model. Section 4 verifies the existence of transcritical bifurcation. Section 5 provides the construction of a numerical procedure based on Newton polynomials. Section 6 provides the simulation through contour and bar plots using the fractal fractional Mittag-Leffler operator. Finally, Section 7 concludes the study.

2. PRELIMINARIES

This subsection presents the fundamental results from [26] which will be used in the remaining part of the study.

Definition 1: The Mittag-Leffler function generalizes the exponential function and plays a crucial role in the solution of fractional DEs.

The Mittag-Leffler function with one and two parameters are defined as:

$$\begin{aligned} \mathcal{E}_{\rho}(z) &= \sum_{k=0}^{\infty} \frac{z^k}{\Gamma(\rho k+1)}, \quad \rho > 0, \\ \mathcal{E}_{\rho,\zeta}(z) &= \sum_{k=0}^{\infty} \frac{z^k}{\Gamma(\rho k+\zeta)}, \quad \rho > 0, \zeta > 0, \end{aligned}$$

where $\Gamma(\cdot)$ shows the Gamma function.

Definition 2: The fractal fractional operator of a function $\mathcal{F}(t)$ with non integer order ρ and fractal dimension ζ in the Mittag Leffler $\mathcal{E}_{\rho}(\cdot)$ sense can be stated as:

$$^{\mathbb{FFM}}D^{\rho,\zeta}\,\mathcal{F}(t) = \frac{\mathcal{M}(\rho)}{1-\rho}\,\frac{d}{dt^{\zeta}}\int_0^t \mathcal{F}(\psi)\,\mathcal{E}_{\rho}\left(-\frac{\rho}{1-\rho}(t-\psi)^{\rho}\right)\,d\psi, \tag{2.1}$$

where $\mathcal{M}(\rho)$ is the normalization function which satisfies $\mathcal{M}(0) = \mathcal{M}(1) = 1$, also consistent with non integer order operators as ζ tends to 1.

Definition 3: Let $\mathcal{F}(t)$ be a continuous function on $(0,\infty)$. The fractal fractional integral of order (ρ,ζ) in the Mittag–Leffler sense is expressed as:

$$^{\mathbb{FFM}}I^{\rho,\zeta}\,\mathcal{F}(t) = \frac{\zeta(1-\rho)}{\mathcal{M}(\rho)}\,t^{\zeta-1}\,\mathcal{F}(t) + \frac{\zeta\rho}{\mathcal{M}(\rho)\,\Gamma(\rho)}\int_0^t (t-\psi)^{\rho-1}\,\psi^{\zeta-1}\,\mathcal{F}(\psi)\,d\psi. \tag{2.2}$$

Definition 4: A point $\mathbf{y}^*$ in a dynamical system $^{\mathbb{FFM}}D^{\rho,\zeta}\mathbf{y} = \mathbf{f}(\mathbf{y})$ is referred to as equilibrium point if $\mathbf{f}(\mathbf{y}^*) = \mathbf{0}$.

Lemma 1: Let $y(t) \in C^1[0,T]$ and $^{\mathbb{FFM}}D^{\rho,\zeta}y(t) \geq 0$ for all $t \in [0,T]$ with non-negative initial state. Then $y(t) \geq 0$ for all $t \in [0,T]$.

3. DESCRIPTION AND FORMULATION OF MODEL

This section explains how the eight-compartment model has been developed and how it describes the dynamics of avian influenza transmission between humans and birds.

The human population has been classified into four groups: susceptible people $(S^{\hbar}(t))$, vaccinated people $(V^{\hbar}(t))$, infected people $(I^{\hbar}(t))$, and recovered people $(R^{\hbar}(t))$, who have acquired immunity after infection. Similarly, the bird population contains susceptible birds $S^b(t)$, vaccinated birds $V^b(t)$, infected birds $I^b(t)$, and recovered birds $R^b(t)$. Biological processes include recruitment, vaccination, infection, natural death, disease-induced death, recovery, and immunity acquisition, which control the transitions between compartments. Immunity against avian influenza is generally not lifelong because vaccine-induced and naturally acquired immunity may decline over time, and antigenic drift of influenza viruses can further reduce long-term protection. To improve the biological reliability of the model, we have assumed that the vaccinated humans and birds again become susceptible at the rate of η and σ. Consequently, vaccinated individuals gradually lose immunity and return to the susceptible compartment. This assumption makes the proposed

model more consistent with the epidemiology of influenza viruses. The susceptible human population grows at a recruitment rate Λ and the rate η at which vaccinated individuals again become susceptible, and declines at rates of bird-to-human transmission β, through vaccination υ, and through the natural death rate μ. Vaccinated humans increase through vaccination rate υ and decrease through natural death μ. New infections increase the infected human class, while disease-induced mortality (α), natural death (μ), and recovery γ cause reductions. Contact with infected birds is the only way for humans to become infected, as reflected through the term $\beta S^{\hbar} I^{b}$. According to WHO data, human-to-human transmission is very low [42]. The recovery of infected individuals causes the number of recovered humans to rise, and the natural death rate μ declines the recovered human population. The susceptible birds increase at the recruitment rate ϕ and the rate σ at which vaccinated birds again become susceptible and decline due to bird-to-bird transmission (χ), vaccination (κ), and the natural mortality rate (Ξ). The vaccinated birds rise as a result of the vaccination of susceptible birds κ, and fall as a result of natural death and movement into the susceptible class. Contact of susceptible birds with infectious birds raises the infected birds population, while disease-induced and natural mortality, as well as recovery, lower it. The recovered birds R^{b} rise due to the recovery rate and decline due to the natural death rate.

The parameter values listed in Table 4 are derived from [27]. Figure 2 displays the

Parameter	**Biological meaning**	**Value**	**Dimension**
Λ	Human recruitment rate	10 person.day^{-1}	[T^{-1}N]
μ	Human natural death rate	0.000039 day^{-1}	[T^{-1}]
υ	Human vaccination rate	0.3 day^{-1}	[T^{-1}]
η	Human vaccine waning rate	0.033 day^{-1}	[T^{-1}]
α	Human disease-induced death rate	0.05 day^{-1}	[T^{-1}]
γ	Human recovery rate	0.36 day^{-1}	[T^{-1}]
β	Bird to human transmission rate	0.015 day^{-1}	[T^{-1}]
ϕ	Bird recruitment rate	10 birds.day^{-1}	[T^{-1}N]
Ξ	Bird natural death rate	0.01 day^{-1}	[T^{-1}]
κ	Bird vaccination rate	0.6 day^{-1}	[T^{-1}]
σ	Bird vaccine waning rate	0.016 day^{-1}	[T^{-1}]
ξ	Bird disease-induced death rate	0.1 day^{-1}	[T^{-1}]
ω	Bird recovery rate	0.3 day^{-1}	[T^{-1}]
χ	Bird-to-bird transmission rate	0.05 day^{-1}	[T^{-1}]

TABLE 4. Parameter values with units and dimensions for the Avian Influenza model

flow chart representing the interaction between various compartments of humans and birds involved in the model: Using the above description of model variables and parameters, we

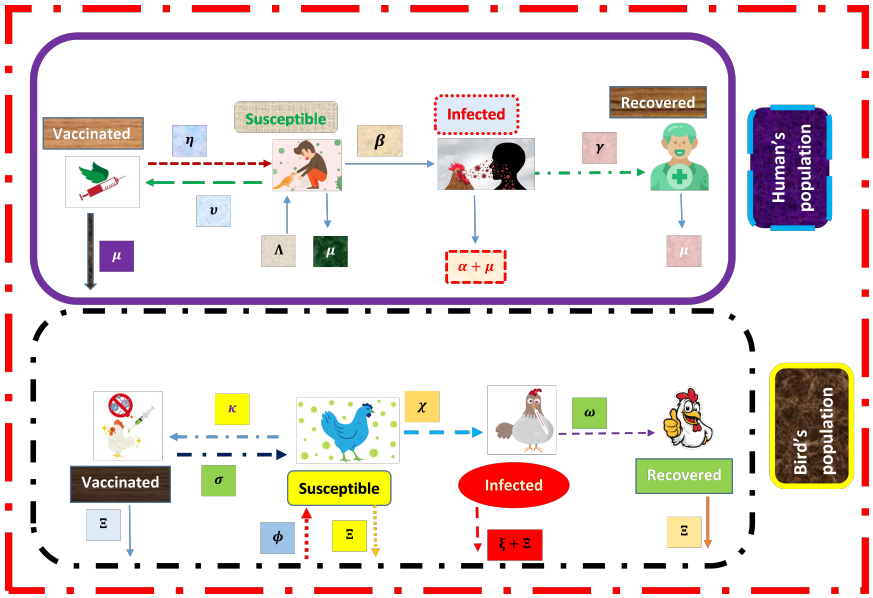

FIGURE 2. Flow chart describing the interactions of various compartments of humans and birds.

present the modified model from [27] as follows:

$$\begin{aligned}
DS^{\hbar}(t) &= \Lambda - \beta S^{\hbar}(t)I^{b}(t) + \eta V^{\hbar}(t) - (\upsilon + \mu)S^{\hbar}(t),\\
DV^{\hbar}(t) &= \upsilon S^{\hbar}(t) - (\eta + \mu)V^{\hbar}(t),\\
DI^{\hbar}(t) &= \beta S^{\hbar}(t)I^{b}(t) - (\alpha + \mu + \gamma)I^{\hbar},\\
DR^{\hbar}(t) &= \gamma I^{\hbar} - \mu R^{\hbar}(t),\\
DS^{b}(t) &= \phi - \chi S^{b}(t)I^{b}(t) + \sigma V^{b}(t) - (\kappa + \Xi)S^{b}(t),\\
DV^{b}(t) &= \kappa S^{b} - (\sigma + \Xi)V^{b}(t),\\
DI^{b}(t) &= \chi S^{b}(t)I^{b}(t) - (\xi + \Xi + \omega)I^{b}(t),\\
DR^{b}(t) &= \omega I^{b}(t) - \Xi R^{b}(t),
\end{aligned} \tag{3.3}$$

where all initial values are non-negative real numbers.

The Mittag-Leffler kernel is chosen over alternatives, as it can be used to describe self-similarities in complex biological systems. The Mittag-Leffler kernel has the same dynamics at different scales, unlike the Caputo-Fabrizio kernel, which has non-index law properties, leading to crossover effects. The fractal-fractional Mittag-Leffler operator has been successfully applied to multiple epidemic models. [22] applied the fractal-fractional operator on a COVID-19 model and concluded that the fractal-fractional order COVID-19 model provides deeper insights into epidemic disease. [41] studied Measles disease with the fractal-fractional derivative and concluded that changes in the fractal-fractional order lead to changes in disease dynamics. [32] studied the dynamics of Chlamydia disease

and concluded that the application of the fractal-fractional operator demonstrates chaotic analysis and qualitative stability. Moreover, the operator also offers second-order accurate numerical schemes that require small calculations of special functions, which is the reason why it could be used in our avian influenza model.

The extension of the integer-order model (3.3) with the application of the fractal-fractional operator in the Mittag-Leffler sense is provided below:

$$\begin{aligned}
{}^{\mathbb{FFM}}D^{\rho,\zeta}S^h(t) &= \Lambda + \eta V^h(t) - \beta S^h(t)I^b(t) - (\upsilon+\mu)S^h(t),\\
{}^{\mathbb{FFM}}D^{\rho,\zeta}V^h(t) &= \upsilon S^h(t) - (\eta+\mu)V^h(t),\\
{}^{\mathbb{FFM}}D^{\rho,\zeta}I^h(t) &= \beta S^h(t)I^b(t) - (\alpha+\mu+\gamma)I^h(t),\\
{}^{\mathbb{FFM}}D^{\rho,\zeta}R^h(t) &= \gamma I^h(t) - \mu R^h(t),\\
{}^{\mathbb{FFM}}D^{\rho,\zeta}S^b(t) &= \phi + \sigma V^b(t) - \chi S^b(t)I^b(t) - (\kappa+\Xi)S^b(t),\\
{}^{\mathbb{FFM}}D^{\rho,\zeta}V^b(t) &= \kappa S^b(t) - (\sigma+\Xi)V^b(t),\\
{}^{\mathbb{FFM}}D^{\rho,\zeta}I^b(t) &= \chi S^b(t)I^b(t) - (\xi+\Xi+\omega)I^b(t),\\
{}^{\mathbb{FFM}}D^{\rho,\zeta}R^b(t) &= \omega I^b(t) - \Xi R^b(t),
\end{aligned} \tag{3.4}$$

where all initial values are non-negative real numbers.

Remark 1: The fractal-fractional derivative is applied to the left-hand side of the equations, and the right-hand side is kept in the same form as the classical equation. This is a common property of the fractal-fractional differential equations and does not mean that the biological systems have been changed, but rather the memory property of the system is modified by the fractional-order (ρ) and the scaling property is modified by the fractal dimension (ζ). The parameter rates are all in units of day$(^{-\rho\zeta})$ in order to be dimensionally consistent.

4. Qualitative and quantitative analysis of model

In this section, we aim to cover the fundamental properties of the model, including the presence of a unique, bounded, and positive solution, equilibrium points, local and global stability of Influenza-free equilibrium points, reproductive number, local and global sensitivity analysis of parameters, statistical analysis, chaos test, and phase plots.

4.1. Existence and uniqueness of solutions.

We establish the existence and uniqueness of solutions for the fractal-fractional order Avian Influenza system (3.4) using the Banach contraction principle. The fractal-fractional derivative with Mittag-Leffler kernel can be expressed in the equivalent Volterra integral form:

$$u(t) = \zeta(1-\rho)t^{\zeta-1}f(t,u(t)) + \frac{\zeta\rho}{\Gamma(\rho)}\int_0^t (t-s)^{\rho-1}s^{\zeta-1}f(s,u(s)),ds,$$

We write the system in the compact form. Let the state vector be:

$$\mathbf{X}(t) = \begin{pmatrix} S^h(t) \\ V^h(t) \\ I^h(t) \\ R^h(t) \\ S^b(t) \\ V^b(t) \\ I^b(t) \\ R^b(t) \end{pmatrix}, \quad \mathbf{X}0 = \begin{pmatrix} S^h(0) \\ V^h(0) \\ I^h(0) \\ R^h(0) \\ S^b(0) \\ V^b(0) \\ I^b(0) \\ R^b(0) \end{pmatrix}.$$

The system (3.4) can be written as:

$$^{\mathbb{FFM}}D^{\rho,\zeta}\mathbf{X}(t) = \mathbf{f}(t, \mathbf{X}(t)), \quad \mathbf{X}(0) = \mathbf{X}0,$$

where $\mathbf{f} : [0, T] \times \mathbb{R}^8+ \to \mathbb{R}^8$ is defined as:

$$\mathbf{f}(t, \mathbf{X}) = \begin{pmatrix} \Lambda + \eta V^h - \beta S^h I^b - \upsilon S^h - \mu S^h \\ \upsilon S^h - \eta V^h - \mu V^h \\ \beta S^h I^b - \alpha I^h - \mu I^h - \gamma I^h \\ \gamma I^h - \mu R^h \\ \phi + \sigma V^b - \chi S^b I^b - \kappa S^b - \Xi S^b \\ \kappa S^b - \sigma V^b - \Xi V^b \\ \chi S^b I^b - \xi I^b - \Xi I^b - \omega I^b \\ \omega I^b - \Xi R^b \end{pmatrix}.$$

We make the following standard assumptions:

(1) The function $\mathbf{f}$ is continuous on $[0, T] \times \mathbb{R}^8+$.

(2) There exists a positive constant $L > 0$ such that for all $\mathbf{X}_1, \mathbf{X}2 \in \mathbb{R}^8+$:

$$|\mathbf{f}(t, \mathbf{X}_1) - \mathbf{f}(t, \mathbf{X}_2)| \leq L|\mathbf{X}1 - \mathbf{X}2|,$$

i.e., $\mathbf{f}$ is Lipschitz continuous with respect to the second variable.

(3) The function $\mathbf{f}$ is bounded. i.e. there exists a positive constant $M > 0$ such that $|\mathbf{f}(t, \mathbf{X})| \leq M$ for all $t \in [0, T]$ and $\mathbf{X} \in \mathbb{R}^8+$.

For our system, the Lipschitz constant L is given by:

$$L = \max \begin{cases} \beta S^h I^b + \upsilon + \mu, & \text{(from } S^h \text{ equation)} \\ \eta + \mu, & \text{(from } V^h \text{ equation)} \\ \alpha + \mu + \gamma, & \text{(from } I^h \text{ equation)} \\ \mu, & \text{(from } R^h \text{ equation)} \\ \chi S^b I^b + \kappa + \Xi, & \text{(from } S^b \text{ equation)} \\ \sigma + \Xi, & \text{(from } V^b \text{ equation)} \\ \xi + \Xi + \omega, & \text{(from } I^b \text{ equation)} \\ \Xi & \text{(from } R^b \text{ equation)} \end{cases}.$$

Since the state variables are bounded, the Lipschitz constant is finite and positive:

$$L = \max\{\beta {S^h}^* {I^b}^* + \upsilon + \mu, \eta + \mu, \alpha + \mu + \gamma, \mu, \chi {S^b}^* {I^b}^* + \kappa + \Xi, \sigma + \Xi, \xi + \Xi + \omega, \Xi\}.$$

Using the fractal-fractional integral operator, the system (3.4) is equivalent to the Volterra integral equation:

$$\mathbf{X}(t) = \mathbf{X}0 + \zeta(1-\rho)t^{\zeta-1}\mathbf{f}(t,\mathbf{X}(t)) + \frac{\rho\zeta}{\Gamma(\rho)}\int_0^t (t-s)^{\rho-1}s^{\zeta-1}\mathbf{f}(s,\mathbf{X}(s))ds.$$

Define the operator $\mathcal{T} : C([0,T],\mathbb{R}^8+) \to C([0,T],\mathbb{R}^8+)$ by:

$$\mathcal{T}\mathbf{X}(t) = \mathbf{X}_0 + \zeta(1-\rho)t^{\zeta-1}\mathbf{f}(t,\mathbf{X}(t)) + \frac{\rho\zeta}{\Gamma(\rho)}\int_0^t (t-s)^{\rho-1}s^{\zeta-1}\mathbf{f}(s,\mathbf{X}(s))ds.$$

Theorem 1: Under the assumptions above, the suggested Avian Influenza system (3.4) has at least one solution on $[0,T]$.

Proof: Let $\mathcal{B}r = \mathbf{X} \in C([0,T],\mathbb{R}^8+) : |\mathbf{X} - \mathbf{X}0| \leq r$ be a closed ball in the Banach space $C([0,T],\mathbb{R}^8+)$ with the supremum norm.

For $\mathbf{X} \in \mathcal{B}_r$:

$$\begin{aligned}|\mathcal{T}\mathbf{X}(t) - \mathbf{X}_0| &\leq \zeta(1-\rho)t^{\zeta-1}|\mathbf{f}(t,\mathbf{X}(t))| + \frac{\rho\zeta}{\Gamma(\rho)}\int_0^t (t-s)^{\rho-1}s^{\zeta-1}|\mathbf{f}(s,\mathbf{X}(s))|ds,\\ &\leq M\left[\zeta(1-\rho)T^{\zeta-1} + \frac{\rho\zeta\Gamma(\zeta)}{\Gamma(\rho+\zeta)}T^{\rho+\zeta-1}\right].\end{aligned}$$

Since $t^{\zeta-1}$ is bounded on $[0,T]$ and the integral is finite, there exists $r > 0$ such that $|\mathcal{T}\mathbf{X}(t) - \mathbf{X}_0| \leq r$. Thus $\mathcal{T}$ maps $\mathcal{B}_r$ into itself.

By the Arzelà-Ascoli theorem, $\mathcal{T}$ is relatively compact, and since $\mathbf{f}$ is continuous, $\mathcal{T}$ is completely continuous. By Schauder's fixed point theorem, $\mathcal{T}$ has at least one fixed point, which is a solution of the integral equation, and hence of the fractal-fractional system. □

Theorem 2: Under the assumptions above, the Avian Influenza model (3.4) has a unique solution on $[0,T]$ provided:

$$\Omega = L\left[\zeta(1-\rho)T^{\zeta-1} + \frac{\rho\zeta\Gamma(\zeta)}{\Gamma(\rho+\zeta)}T^{\rho+\zeta-1}\right] < 1.$$

Proof: For any $\mathbf{X}_1, \mathbf{X}2 \in C([0,T],\mathbb{R}^8+)$:

$$\begin{aligned}|\mathcal{T}\mathbf{X}_1(t) - \mathcal{T}\mathbf{X}_2(t)| &\leq \zeta(1-\rho)t^{\zeta-1}|\mathbf{f}(t,\mathbf{X}_1(t)) - \mathbf{f}(t,\mathbf{X}_2(t))|\\ &\quad + \frac{\rho\zeta}{\Gamma(\rho)}\int_0^t (t-s)^{\rho-1}s^{\zeta-1}|\mathbf{f}(s,\mathbf{X}_1(s)) - \mathbf{f}(s,\mathbf{X}_2(s))|ds.\end{aligned}$$

Using the Lipschitz condition:

$$\begin{aligned}|\mathcal{T}\mathbf{X}_1(t) - \mathcal{T}\mathbf{X}_2(t)| &\leq L|\mathbf{X}_1 - \mathbf{X}_2|\left[\zeta(1-\rho)t^{\zeta-1} + \frac{\rho\zeta}{\Gamma(\rho)}\int_0^t (t-s)^{\rho-1}s^{\zeta-1}ds\right]\\ &= L|\mathbf{X}_1 - \mathbf{X}_2|\left[\zeta(1-\rho)t^{\zeta-1} + \frac{\rho\zeta\Gamma(\zeta)}{\Gamma(\rho+\zeta)}t^{\rho+\zeta-1}\right].\end{aligned}$$

Taking the supremum over $t \in [0,T]$:

$$|\mathcal{T}\mathbf{X}_1 - \mathcal{T}\mathbf{X}_2| \leq L\left[\zeta(1-\rho)T^{\zeta-1} + \frac{\rho\zeta\Gamma(\zeta)}{\Gamma(\rho+\zeta)}T^{\rho+\zeta-1}\right]|\mathbf{X}_1 - \mathbf{X}_2|.$$

Thus:

$$|\mathcal{T}\mathbf{X}_1 - \mathcal{T}\mathbf{X}_2| \leq \Omega|\mathbf{X}_1 - \mathbf{X}_2|,$$

where

$$\Omega = L\left[\zeta(1-\rho)T^{\zeta-1} + \frac{\rho\zeta\Gamma(\zeta)}{\Gamma(\rho+\zeta)}T^{\rho+\zeta-1}\right] < 1.$$

Since $\Omega < 1$, $\mathcal{T}$ is a contraction. By the Banach contraction principle, $\mathcal{T}$ has a unique fixed point, which is the unique solution of the fractal-fractional system. □

Corollary 1: The fractal-fractional avian influenza model (3.4) has a unique solution for all $t \geq 0$ in the biologically feasible region Ω.

Remark 2: The contraction condition $\Omega < 1$ can always be satisfied by choosing a sufficiently small final time T. For larger time intervals, the existence and uniqueness can be extended by continuation arguments, as is standard in the theory of fractional differential equations.

4.2. **Positivity and boundedness.** In this part, we establish the biological feasibility of the fractal-fractional model by proving that all solutions remain non-negative and bounded for all time $t \geq 0$, provided the initial conditions are non-negative. This ensures the biological feasibility of the model. In addition to eliminating unrealistic exponential growth and guaranteeing the long-term prediction capability of the model, the boundedness property verifies that the overall population stays finite.

Theorem 3: For any non-negative initial conditions, the solutions of system (3.4) remain non-negative for all $t \geq 0$.

Proof: We prove step by step positivity for each compartment.

From the First equation of the system (3.4), we have

$$^{\mathbb{FFM}}D^{\rho,\zeta}S^h(t) = \Lambda + \eta V^h(t) - (\beta I^b(t) + \upsilon + \mu)S^h(t).$$

Assume for contradiction that there exists a first time $t_1 > 0$ such that $S^h(t_1) = 0$ and $S^h(t) > 0$ for $t \in [0, t_1)$. Then:

$$^{\mathbb{FFM}}D^{\rho,\zeta}S^h(t_1) = \Lambda + \eta V^h(t_1) \geq 0,$$

since $V^h(t_1) \geq 0$ and all parameters are positive.

By Lemma 1, this implies $S^h(t) \geq 0$ for all $t \geq 0$.

From the expression of vaccinated humans, we have:

$$^{\mathbb{FFM}}D^{\rho,\zeta}V^h(t) = \upsilon S^h(t) - (\eta + \mu)V^h(t).$$

Since $S^h(t) \geq 0$ and $\upsilon > 0$, we have:

$$^{\mathbb{FFM}}D^{\rho,\zeta}V^h(t) \geq -(\eta + \mu)V^h(t).$$

By the fractional Gronwall inequality, this implies:

$$V^h(t) \geq V^h(0)\mathcal{E}\rho(-(\eta+\mu)t^\rho) \geq 0,$$

where $\mathcal{E}\rho$ is the Mittag-Leffler function. Hence $V^h(t) \geq 0$ for all $t \geq 0$.

From the Third equation of the model (3.4), we have:

$$^{\mathbb{FFM}}D^{\rho,\zeta}I^h(t) = \beta S^h(t)I^b(t) - (\alpha + \mu + \gamma)I^h(t).$$

Since $S^h(t) \geq 0$ and $I^b(t) \geq 0$, and $\beta > 0$:

$$^{\mathbb{FFM}}D^{\rho,\zeta}I^h(t) \geq -(\alpha + \mu + \gamma)I^h(t).$$

By the fractional Gronwall inequality, we obtain the following expression:

$$I^h(t) \geq I^h(0)\mathcal{E}\rho(-(\alpha+\mu+\gamma)t^\rho) \geq 0.$$

Hence $I^h(t) \geq 0$ for all $t \geq 0$. From the fourth equation of recovered humans, we have

$$^{\mathbb{FFM}}D^{\rho,\zeta}R^h(t) = \gamma I^h(t) - \mu R^h(t).$$

Since $I^h(t) \geq 0$:

$$^{\mathbb{FFM}}D^{\rho,\zeta}R^h(t) \geq -\mu R^h(t).$$

By the fractional Gronwall inequality:

$$R^h(t) \geq R^h(0)\mathcal{E}\rho(-\mu t^\rho) \geq 0.$$

Hence $R^h(t) \geq 0$ for all $t \geq 0$.

In a similar pattern, we verify the positivity of the bird compartments. From the Fifth equation of the system 3.4:

$$^{\mathbb{FFM}}D^{\rho,\zeta}S^b(t) = \phi + \sigma V^b(t) - (\chi I^b(t) + \kappa + \Xi)S^b(t).$$

Assume there exists a first time $t_2 > 0$ such that $S^b(t_2) = 0$ and $S^b(t) > 0$ for $t \in [0, t_2)$. Then:

$$^{\mathbb{FFM}}D^{\rho,\zeta}S^b(t_2) = \phi + \sigma V^b(t_2) \geq 0.$$

By Lemma 1, $S^b(t) \geq 0$ for all $t \geq 0$.

From the Sixth equation of the system (3.4), we have:

$$^{\mathbb{FFM}}D^{\rho,\zeta}V^b(t) = \kappa S^b(t) - (\sigma + \Xi)V^b(t).$$

Since $S^b(t) \geq 0$ and $\kappa > 0$:

$$^{\mathbb{FFM}}D^{\rho,\zeta}V^b(t) \geq -(\sigma + \Xi)V^b(t).$$

By the fractional Gronwall inequality:

$$V^b(t) \geq V^b(0)\mathcal{E}_\rho(-(\sigma + \Xi)t^\rho) \geq 0.$$

Hence $V^b(t) \geq 0$ for all $t \geq 0$.

From the Seventh equation of the system (3.4), we have:

$$^{\mathbb{FFM}}D^{\rho,\zeta}I^b(t) = \chi S^b(t)I^b(t) - (\xi + \Xi + \omega)I^b(t).$$

Since $S^b(t) \geq 0$ and $\chi > 0$:

$$^{\mathbb{FFM}}D^{\rho,\zeta}I^b(t) \geq -(\xi + \Xi + \omega)I^b(t).$$

By the fractional Gronwall inequality:

$$I^b(t) \geq I^b(0)\mathcal{E}_\rho(-(\xi + \Xi + \omega)t^\rho) \geq 0.$$

Hence $I^b(t) \geq 0$ for all $t \geq 0$.

From the eighth equation of the system (3.4), we have:

$$^{\mathbb{FFM}}D^{\rho,\zeta}R^b(t) = \omega I^b(t) - \Xi R^b(t).$$

Since $I^b(t) \geq 0$:

$$^{\mathbb{FFM}}D^{\rho,\zeta}R^b(t) \geq -\Xi R^b(t).$$

By the fractional Gronwall inequality:

$$R^b(t) \geq R^b(0)\mathcal{E}_\rho(-\Xi t^\rho) \geq 0.$$

Hence $R^b(t) \geq 0$ for all $t \geq 0$.

Thus, all solutions remain non-negative for all $t \geq 0$. □

Theorem 4: All solutions of system (3.4) with non-negative initial conditions are bounded for all $t \geq 0$.

Proof: We first establish the boundedness of the total human population $N^h(t) = S^h(t) + V^h(t) + I^h(t) + R^h(t)$. Summing the first four equations of the system (3.4), we have:

$$\begin{aligned} {}^{\mathbb{FFM}}D^{\rho,\zeta}N^h(t) &= \Lambda - \mu(S^h + V^h + I^h + R^h) - \alpha I^h(t), \\ &\leq \Lambda - \mu N^h(t). \end{aligned}$$

Applying the fractional Gronwall inequality:

$$N^h(t) \leq \frac{\Lambda}{\mu} + \left(N^h(0) - \frac{\Lambda}{\mu}\right)\mathcal{E}\rho(-\mu t^\rho).$$

Since the Mittag-Leffler function satisfies $0 < \mathcal{E}\rho(-z) \leq 1$ for $z \geq 0$:

$$N^h(t) \leq \max\left\{N^h(0), \frac{\Lambda}{\mu}\right\}.$$

Similarly, for the total bird population $N^b(t) = S^b(t) + V^b(t) + I^b(t) + R^b(t)$:

Summing equations of bird compartments of the system (3.4), we have

$$\begin{aligned} {}^{\mathbb{FFM}}D^{\rho,\zeta}N^b(t) &= \phi - \Xi(S^b + V^b + I^b + R^b) - \xi I^b(t), \\ &\leq \phi - \Xi N^b(t). \end{aligned}$$

Applying the fractional Gronwall inequality:

$$N^b(t) \leq \frac{\phi}{\Xi} + \left(N^b(0) - \frac{\phi}{\Xi}\right)\mathcal{E}_\rho(-\Xi t^\rho) \leq \max\left\{N^b(0), \frac{\phi}{\Xi}\right\}.$$

Thus, both human and bird populations are bounded for all $t \geq 0$, and consequently all state variables are bounded. □

Corollary 2: The biologically feasible region:

$$\Omega = \left\{(S^h, V^h, I^h, R^h, S^b, V^b, I^b, R^b) \in \mathbb{R}^8_+ : N^h \leq \frac{\Lambda}{\mu}, \quad N^b \leq \frac{\phi}{\Xi}\right\}.$$

is positively invariant for the fractal-fractional model. Biologically, the above theorems describe the ratio of the birth rate to the natural mortality rate bounded by the total population of both humans and animals. This indicates the biological feasibility of the suggested model.

4.3. **Equilibrium points.** We examine the equilibrium points of the Influenza model (3.4) by setting all of the derivatives of the system to zero in order to understand its long-term behavior. In the coupled humans and birds populations, we obtain two equilibrium points, where infection persists or is eliminated, known as disease-free and endemic states. The Influenza-free equilibrium points where infection is eliminated are given by:

$$E^0 = \left(\frac{\Lambda(\eta+\mu)}{\mu(\eta+\mu+\upsilon)}, \frac{\upsilon\Lambda}{\mu(\eta+\mu+\upsilon)}, 0, 0, \frac{\phi(\Xi+\sigma)}{\Xi(\kappa+\Xi+\sigma)}, \frac{\kappa\phi}{\Xi(\kappa+\Xi+\sigma)}, 0, 0\right).$$

4.4. **Positivity conditions for endemic equilibrium.** The endemic equilibrium of system (3.4) is biologically meaningful when all the endemic equilibrium points are strictly positive. In this part, we derive the positivity condition for endemic equilibrium points denoted by:

$$E^* = (S^{h^*}, V^{h^*}, I^{h^*}, R^{h^*}, S^{b^*}, V^{b^*}, I^{b^*}, R^{b^*}) \in \mathbb{R}^8_+.$$

The influenza-persistent equilibrium points obtained by equating the right-hand side of the system (3.4) to zero and then solving for positive values of infected compartments are given by:

$$S^{h^*} = \frac{\Lambda}{\beta I^{b^*} + \frac{\mu(\upsilon+\eta+\mu)}{\eta+\mu}}. \tag{4.5}$$

$$V^{h^*} = \frac{\upsilon S^{h^*}}{\eta+\mu}. \tag{4.6}$$

$$I^{h^*} = \frac{\beta S^{h^*} I^{b^*}}{\alpha+\mu+\gamma}. \tag{4.7}$$

$$R^{h^*} = \frac{\gamma I^{h^*}}{\mu}. \tag{4.8}$$

$$S^{b^*} = \frac{\xi+\Xi+\omega}{\chi}. \tag{4.9}$$

$$V^{b^*} = \frac{\kappa(\xi+\Xi+\omega)}{\chi(\sigma+\Xi)}. \tag{4.10}$$

$$I^{b^*} = \frac{\phi\chi + \frac{\sigma\kappa(\xi+\Xi+\omega)}{(\sigma+\Xi)} - (\kappa+\Xi)(\xi+\Xi+\omega)}{\chi(\xi+\Xi+\omega)}. \tag{4.11}$$

$$R^{b^*} = \frac{\omega I^{b^*}}{\Xi}. \tag{4.12}$$

For the endemic equilibrium to be biologically meaningful, all components must be strictly positive:

$$S^{h^*} > 0, \quad V^{h^*} > 0, \quad I^{h^*} > 0, \quad R^{h^*} > 0, \quad S^{b^*} > 0, \quad V^{b^*} > 0, \quad I^{b^*} > 0, \quad R^{b^*} > 0.$$

Condition 1 is imposed on bird compartments. From equation (4.9), since $\chi > 0$:

$$S^{b^*} > 0 \iff \xi+\Xi+\omega > 0,$$

which is always true as all parameters are positive.

From equation (4.10):

$$V^{b^*} > 0 \iff \kappa > 0,$$

which is true by definition.

From expression (4.12):

$$R^{b^*} > 0 \iff I^{b^*} > 0.$$

Condition 2 is imposed on human compartments for the positivity of equilibrium points. From expression (4.5), the denominator must be positive:

$$\beta I^{b^*} + \frac{\mu(\upsilon + \eta + \mu)}{\eta + \mu} > 0,$$

which is always true since all terms are positive.

From equation (4.6):

$$V^{h^*} > 0 \quad \Longleftrightarrow \quad S^{h^*} > 0,$$

which is true by the above.

From equation (4.7), $I^{h^*} > 0$ requires:

$$S^{h^*} > 0 \quad \text{and} \quad I^{b^*} > 0.$$

Both conditions are satisfied by the preceding results. From equation (4.8):

$$R^{h^*} > 0 \quad \Longleftrightarrow \quad I^{h^*} > 0,$$

which is true by the above.

From the above analysis, it can be noticed that the endemic equilibrium exists when the bird population can sustain transmission in spite of natural mortality, disease-induced mortality, recovery, and vaccination. After bird infection, the human compartments are positive, which is in accordance with the zoonotic nature of avian influenza. The fractal-fractional parameters ρ and ζ are not present in the equilibrium conditions, but rather they influence the dynamics, but not the values of the equilibrium points. However, they have a significant impact on the stability and convergence properties of the endemic equilibrium of the model.

4.5. **Reproductive number.** Using the next-generation matrix approach, we determine the basic reproduction number $\mathcal{R}_0$ to evaluate the risk of disease elimination and persistence in the human and bird populations. The system is divided into two parts: the matrix F, which shows the emergence of new infections in each compartment, and the matrix V, which records the rates of transitions in and out of infected compartments, including recovery, death, and other non-infectious flows. The reproduction number measures the number of new infected birds that can be produced by a single infected bird in a susceptible population, is obtained from the spectral radius of the matrix FV^{-1}. The F and V matrices for the proposed avian influenza model are:

$$F = \begin{pmatrix} 0 & 0 & 0 & 0 & 0 & 0 & 0 & 0 \\ 0 & 0 & 0 & 0 & 0 & 0 & 0 & 0 \\ 0 & 0 & 0 & 0 & 0 & 0 & \frac{\beta(\Lambda(\eta+\mu))}{\mu(\eta+\mu+\upsilon)} & 0 \\ 0 & 0 & 0 & 0 & 0 & 0 & 0 & 0 \\ 0 & 0 & 0 & 0 & 0 & 0 & 0 & 0 \\ 0 & 0 & 0 & 0 & 0 & 0 & 0 & 0 \\ 0 & 0 & 0 & 0 & 0 & 0 & \frac{\chi(\phi(\Xi+\sigma))}{\Xi(\kappa+\Xi+\sigma)} & 0 \\ 0 & 0 & 0 & 0 & 0 & 0 & 0 & 0 \end{pmatrix},$$

and

$$V = \begin{pmatrix} \mu+\upsilon & \eta & 0 & 0 & 0 & 0 & \frac{\beta(\Lambda(\eta+\mu))}{\mu(\eta+\mu+\upsilon)} & 0 \\ -\upsilon & \eta+\mu & 0 & 0 & 0 & 0 & 0 & 0 \\ 0 & 0 & \alpha+\gamma+\mu & 0 & 0 & 0 & 0 & 0 \\ 0 & -\eta & -\gamma & \mu & 0 & 0 & 0 & 0 \\ 0 & 0 & 0 & 0 & \Xi+\kappa & -\sigma & \frac{\chi(\phi(\Xi+\sigma))}{\Xi(\kappa+\Xi+\sigma)} & 0 \\ 0 & 0 & 0 & 0 & -\kappa & \Xi+\sigma & 0 & 0 \\ 0 & 0 & 0 & 0 & 0 & 0 & \Xi+\omega+\xi & 0 \\ 0 & 0 & 0 & 0 & 0 & 0 & -\omega & \Xi \end{pmatrix}.$$

The characteristic equation obtained from the matrix $K = FV^{-1}$ is

$$P(\lambda) = -\lambda^7 \left(\frac{\chi\phi(\Xi+\sigma)}{\Xi(\kappa+\Xi+\sigma)(\xi+\Xi+\omega)} - \lambda \right).$$

The maximum eigenvalue obtained from the characteristic polynomial, named the basic reproduction number, is:

$$\mathcal{R}_0 = \frac{\chi\phi(\Xi+\sigma)}{\Xi(\kappa+\Xi+\sigma)(\xi+\Xi+\omega)}.$$

Biologically, it symbolizes the equilibrium between the recruitment of birds ϕ and the losses resulting from disease-induced mortality ξ, natural death Ξ, vaccination κ, and recovery ω. Infections in birds stop, and the likelihood of zoonotic transmission decreases when $\mathcal{R}_0 < 1$. Outbreaks and human transmission occur when $\mathcal{R}_0 > 1$.

Now, we consider some special cases. If vaccine is not available, that is ($\kappa = 0$), then the reproductive number becomes:

$$\mathcal{R}_0 = \frac{\chi\phi}{\Xi(\xi+\Xi+\omega)}.$$

This is the classical result for avian influenza models.

In this case, vaccine waning is ignored, so ($\sigma = 0$). Then vaccination reduces the susceptible population and thus the reproductive number is also reduced, given in the form:

$$\mathcal{R}_0 = \frac{\chi\phi}{(\kappa+\Xi)(\xi+\Xi+\omega)}.$$

If vaccination is perfect, for which $\kappa \to \infty$, then reproductive number $\mathcal{R}_0 \to 0$. Thus vaccination completely eliminates transmission.

4.6. **Local stability of Influenza-free equilibrium points.** In this part, we linearize the system (3.4) around the Influenza-free equilibrium points and compute the jacobian matrix in order to evaluate the local stability of the Influenza free equilibrium points. The evaluation of the jacobian at the influenza-free equilibrium points shows that small perturbations in each compartment change with time. The eigenvalues obtained through this jacobian determine whether these perturbations increase or decrease, which establishes whether the Influenza-free equilibrium point is locally asymptotically stable. The jacobian matrix for

the Avian influenza model at the Influenza-free equilibrium points has the form:

$$J(E^0) = \begin{bmatrix} -\mu-\upsilon & \eta & 0 & 0 & 0 & 0 & -\frac{\beta(\Lambda(\eta+\mu))}{\mu(\eta+\mu+\upsilon)} & 0 \\ \upsilon & -\eta-\mu & 0 & 0 & 0 & 0 & 0 & 0 \\ 0 & 0 & -\alpha-\gamma-\mu & 0 & 0 & 0 & \frac{\beta(\Lambda(\eta+\mu))}{\mu(\eta+\mu+\upsilon)} & 0 \\ 0 & \eta & \gamma & -\mu & 0 & 0 & 0 & 0 \\ 0 & 0 & 0 & 0 & -\Xi-\kappa & \sigma & -\frac{\chi(\phi(\Xi+\sigma))}{\Xi(\kappa+\Xi+\sigma)} & 0 \\ 0 & 0 & 0 & 0 & \kappa & -\Xi-\sigma & 0 & 0 \\ 0 & 0 & 0 & 0 & 0 & 0 & \frac{\chi(\phi(\Xi+\sigma))}{\Xi(\kappa+\Xi+\sigma)} -\Xi-\omega-\xi & 0 \\ 0 & 0 & 0 & 0 & 0 & 0 & \omega & -\Xi \end{bmatrix}.$$

The characteristic equation obtained from above jacobian matrix generates the following eigenvalues:

$$\lambda_1 = -\mu, \lambda_2 = -\mu, \lambda_3 = -\alpha-\gamma-\mu, \lambda_4 = -\Xi, \lambda_5 = -\Xi, \lambda_6 = -\kappa-\Xi-\sigma,$$
$$\lambda_7 = -\eta-\mu-\upsilon, \lambda_8 = -\frac{\kappa\Xi(\xi+\Xi+\omega)+(\Xi+\sigma)(\Xi(\xi+\Xi+\omega)-\chi\phi)}{\Xi(\kappa+\Xi+\sigma)}.$$

We can see that the first seven eigenvalues are negative because of the biological assumption that all rates of vaccination, disease-induced death, recovery, and natural mortality are positive.

The threshold behavior of the bird population is determined by the eighth eigenvalue

$$\lambda_8 = -\frac{\kappa\Xi(\xi+\Xi+\omega)+(\Xi+\sigma)(\Xi(\xi+\Xi+\omega)-\chi\phi)}{\Xi(\kappa+\Xi+\sigma)}.$$

It is easy to check that this eigenvalue is negative if

$$\mathcal{R}_0 = \frac{\chi\phi(\Xi+\sigma)}{\Xi(\kappa+\Xi+\sigma)(\xi+\Xi+\omega)} < 1. \tag{4.13}$$

In terms of biology, this finding suggests that when both the human and bird reproduction numbers are less than one, the disease-free equilibrium is locally stable. λ_8 can be effectively driven negative by decreasing the bird-to-bird transmission rate (χ), increasing bird vaccination (κ), improving bird recovery (ω), or controlling their recruitment rate (ϕ). This will prevent an outbreak in the bird reservoir and in the human population.

4.7. **Local stability via Routh-Hurwitz criterion.** Now, we verify the local stability of the influenza-free equilibrium using the Routh-Hurwitz criterion.

The characteristic equation from the jacobian matrix is:

$$\det(J(E^0) - \lambda I) = 0.$$

Due to the block diagonal structure of the jacobian, we factor the characteristic polynomial into:

$$P(\lambda) = P_1(\lambda) \cdot P_2(\lambda) \cdot P_3(\lambda) \cdot P_4(\lambda) = 0,$$

where:

$$P_1(\lambda) = (\lambda+\upsilon+\mu)(\lambda+\eta+\mu) - \upsilon\eta,$$
$$P_2(\lambda) = (\lambda+\alpha+\mu+\gamma)(\lambda+\mu),$$
$$P_3(\lambda) = (\lambda+\kappa+\Xi)(\lambda+\Xi+\sigma) - \kappa\sigma,$$
$$P_4(\lambda) = \lambda - \chi S^b{}_0 + (\xi+\Xi+\omega).$$

Now, we apply the Routh-Hurwitz approach for each factor.

Expanding the factor 1: $P_1(\lambda)$, we have

$$P_1(\lambda) = \lambda^2 + (\upsilon + \eta + 2\mu)\lambda + (\upsilon + \mu)(\eta + \mu) - \upsilon\eta.$$

The above expression can be written in the form:

$$P_1(\lambda) = \lambda^2 + a_1^{(1)}\lambda + a_0^{(1)},$$

where:

$$a_1^{(1)} = \upsilon + \eta + 2\mu > 0,$$
$$a_0^{(1)} = (\upsilon + \mu)(\eta + \mu) - \upsilon\eta = \mu(\upsilon + \eta + \mu) > 0.$$

Since $a_1^{(1)}$ and $a_0^{(1)}$ are both positive due to the positivity of the parameters, both roots have negative real parts.

The two roots from the second factor $P_2(\lambda)$ are:

$$\lambda_1 = -(\alpha + \mu + \gamma) < 0, \lambda_2 = -\mu < 0.$$

Both roots are negative, obviously.

Expanding the third factor $P_3(\lambda)$, we have:

$$P_3(\lambda) = \lambda^2 + (\kappa + 2\Xi + \sigma)\lambda + (\kappa + \Xi)(\Xi + \sigma) - \kappa\sigma.$$

The above expression can be written as:

$$P_3(\lambda) = \lambda^2 + a_1^{(3)}\lambda + a_0^{(3)},$$

where:

$$a_1^{(3)} = \kappa + 2\Xi + \sigma > 0,$$
$$a_0^{(3)} = (\kappa + \Xi)(\Xi + \sigma) - \kappa\sigma = \Xi(\kappa + \Xi + \sigma) > 0.$$

Since $a_1^{(3)}$ and $a_0^{(3)}$ are positive, both roots have negative real parts.

The single root from the factor 4: $P_4(\lambda)$ is:

$$\lambda_8 = \chi {S^b}_0 - (\xi + \Xi + \omega).$$

For stability, the root λ_8 should be negative:

$$\chi {S^b}_0 < \xi + \Xi + \omega.$$

Substituting ${S^b}_0 = \dfrac{\phi(\Xi + \sigma)}{\Xi(\kappa + \Xi + \sigma)}$, we obtain the expression:

$$\frac{\chi\phi(\Xi + \sigma)}{\Xi(\kappa + \Xi + \sigma)} < \xi + \Xi + \omega.$$

This can be written as:

$$\mathcal{R}_0 = \frac{\chi\phi(\Xi + \sigma)}{\Xi(\kappa + \Xi + \sigma)(\xi + \Xi + \omega)} < 1.$$

Theorem 6: The Influenza-free equilibrium E^0 is locally stable if $\mathcal{R}_0 < 1$ and unstable if $\mathcal{R}_0 > 1$.

Proof: The Routh-Hurwitz conditions for all four factors are satisfied when $\mathcal{R}_0 < 1$:

(1) $P_1(\lambda)$: $a_1^{(1)} = \upsilon + \eta + 2\mu > 0$, $a_0^{(1)} = \mu(\upsilon + \eta + \mu) > 0$.
(2) $P_2(\lambda)$: Roots are $-(\alpha + \mu + \gamma)$ and $-\mu$, both negative.
(3) $P_3(\lambda)$: $a_1^{(3)} = \kappa + 2\Xi + \sigma > 0$, $a_0^{(3)} = \Xi(\kappa + \Xi + \sigma) > 0$.
(4) $P_4(\lambda)$: $\lambda_8 = (\xi + \Xi + \omega)(\mathcal{R}_0 - 1) < 0$ when $\mathcal{R}_0 < 1$.

The above analysis shows that all eigenvalues have negative real parts, and the Influenza-free equilibrium point is locally asymptotically stable. □

When the bird reproduction number is below unity, then the capacity for bird to bird transmission (χ) and recruitment (ϕ) is not large enough to overcome the natural mortality of birds (Ξ), the mortality induced by disease (ξ), recovery rate of birds (ω), and the effectiveness of bird vaccination (κ), the analysis shows that the Influenza-free equilibrium point will remain stable. This is in accordance with the biological assumption that bird control plays a key role in preventing human spillover. The fractional-order and fractal dimension ρ and ζ do not impact the local stability of the Influenza-free equilibrium point.

4.8. **Global stability of Influenza-free equilibrium.** In this part, we establish the global asymptotic stability of the Influenza-free equilibrium using a suitable Lyapunov function. This strengthens the theoretical contribution by showing that the disease dies out regardless of initial conditions when the reproduction number is below unity.

Theorem 7: The Influenza-free equilibrium E^0 is globally stable in the biologically feasible region Ω if $\mathcal{R}_0 < 1$.

Proof: Consider the Lyapunov function:

$$\mathcal{L}(t) = I^b(t) + \frac{\beta {S^h}_0}{\alpha + \mu + \gamma} I^h(t).$$

Applying the fractal-fractional derivative along the trajectories and substituting the values of the derivative from the system (3.4), we obtain the expression:

$$\begin{aligned} {}^{\mathbb{FF}M}D^{\rho,\zeta}\mathcal{L}(t) &= [\chi S^b - (\xi + \Xi + \omega)]I^b + \frac{\beta {S^h}_0}{\alpha + \mu + \gamma}[\beta S^h I^b - (\alpha + \mu + \gamma)I^h], \\ &= [\chi S^b - (\xi + \Xi + \omega)]I^b + \frac{\beta^2 {S^h}_0 S^h}{\alpha + \mu + \gamma} I^b - \beta {S^h}_0 I^h. \end{aligned}$$

Using the bounds $S^b \leq {S^b}_0$ and $S^h \leq {S^h}_0$ in the above expression, we obtain:

$$\begin{aligned} {}^{\mathbb{FF}M}D^{\rho,\zeta}\mathcal{L}(t) &\leq [\chi {S^b}_0 - (\xi + \Xi + \omega)]I^b + \frac{\beta^2 ({S^h}_0)^2}{\alpha + \mu + \gamma} I^b - \beta {S^h}_0 I^h, \\ &= (\xi + \Xi + \omega)(\mathcal{R}_0 - 1)I^b + \frac{\beta^2 ({S^h}_0)^2}{\alpha + \mu + \gamma} I^b - \beta {S^h}_0 I^h. \end{aligned}$$

When $\mathcal{R}_0 < 1$, ${}^{\mathbb{FF}M}D^{\rho,\zeta}\mathcal{L}(t) \leq 0$ with equality if and only if $I^b = 0$ and $I^h = 0$. By LaSalle's invariance principle for fractional systems, every trajectory starting in Ω converges to E^0 as $t \to \infty$. □

Biologically, when both reproduction numbers are below unity, the Influenza-free equilibrium is globally stable, meaning the disease will die out from both populations irrespective of the initial outbreak size. The fractional-order and fractal dimension do not affect the stability conditions; they only influence the convergence rate to the Influenza-free equilibrium point. As compared to the systems with backward bifurcation, decreasing $\mathcal{R}_0$ below

1 also leads to the eradication of the disease without any extra control measures. Control of $\mathcal{R}_0$ via biosecurity, vaccination, and movement restrictions will be the most effective approach to controlling the system, as this is driven by bird transmission.

4.9. **Sensitivity analysis.** Sensitivity analysis is a crucial mathematical tool that evaluates the importance of various parameters in disease transmission dynamics. This methodology assesses the robustness of model predictions by quantifying how uncertainties in parameter values, often arising from data collection errors or estimation inaccuracies, affect key epidemiological outputs. The normalized forward sensitivity index measures the relative change in the basic reproduction number $\mathcal{R}_0$ per unit relative change in a parameter. When $\mathcal{R}_0$ is a differentiable function of parameter q, this index can be computed using partial derivatives defined by [20]: $\Upsilon_q^{\mathcal{R}_0} = \frac{\partial \mathcal{R}_0}{\partial q} \times \frac{q}{\mathcal{R}_0}$. The resulting sensitivity values, whether constant or complex expressions involving multiple parameters, identify critical parameters requiring precise estimation. Highly sensitive parameters demand careful measurement since minor variations cause substantial changes in model outcomes, while less sensitive parameters tolerate greater estimation uncertainty without significantly affecting predictions, thereby guiding efficient resource allocation in both parameter estimation and intervention planning.

$$
\begin{aligned}
\Upsilon_{\Xi}^{\mathcal{R}_0} &= -\frac{\kappa\left(\sigma(\xi+\omega)+\Xi^2+2\Xi\sigma\right)+(\Xi+\sigma)^2(\xi+2\Xi+\omega)}{(\Xi+\sigma)(\kappa+\Xi+\sigma)(\xi+\Xi+\omega)},\\
\Upsilon_{\sigma}^{\mathcal{R}_0} &= \frac{\kappa\sigma}{(\Xi+\sigma)(\kappa+\Xi+\sigma)},\\
\Upsilon_{\phi}^{\mathcal{R}_0} &= 1,\\
\Upsilon_{\chi}^{\mathcal{R}_0} &= 1,\\
\Upsilon_{\kappa}^{\mathcal{R}_0} &= -\frac{\kappa}{\kappa+\Xi+\sigma},\\
\Upsilon_{\xi}^{\mathcal{R}_0} &= -\frac{\xi}{\xi+\Xi+\omega},\\
\Upsilon_{\omega}^{\mathcal{R}_0} &= -\frac{\omega}{\xi+\Xi+\omega}.
\end{aligned}
$$

The model parameters show significant directional influences on the dynamics of disease transmission based on the sensitivity analysis of the basic reproduction number $\mathcal{R}_0$.

We conduct a sensitivity analysis in order to determine the most important parameters influencing the transmission of disease, providing important information about the best ways to intervene by quantifying the impact of minor changes in the input parameters on $\mathcal{R}_0$. Figure 3a shows that if the bird-to-bird transmission increases, or bird recruitment increases, then the reproductive number $\mathcal{R}_0$ increases. Figure 3b shows that increasing bird mortality or vaccination decreases $\mathcal{R}_0$. However, Figure 3c displays that the higher the proportion of deaths or recovery due to disease lowers the reproductive number $\mathcal{R}_0$. The relationship between transmission and mortality is shown in Figure 3d, revealing that higher mortality can be compensated by higher transmission. Figure 3e shows that vaccination is an effective countermeasure to the effects of high recruitment. From Figure 3f it is clear that recovery and vaccination both lead to a decrease in $\mathcal{R}_0$. The red contour line $\mathcal{R}_0 = 1$ is a critical boundary. Values above the line ($\mathcal{R}_0 > 1$) show that the disease

persists, and values below the line ($\mathcal{R}_0 < 1$) show that the disease can be eliminated from society. The results show that interventions aimed at controlling bird-to-bird transmission (χ) and vaccination (κ) are the best way to control avian influenza.

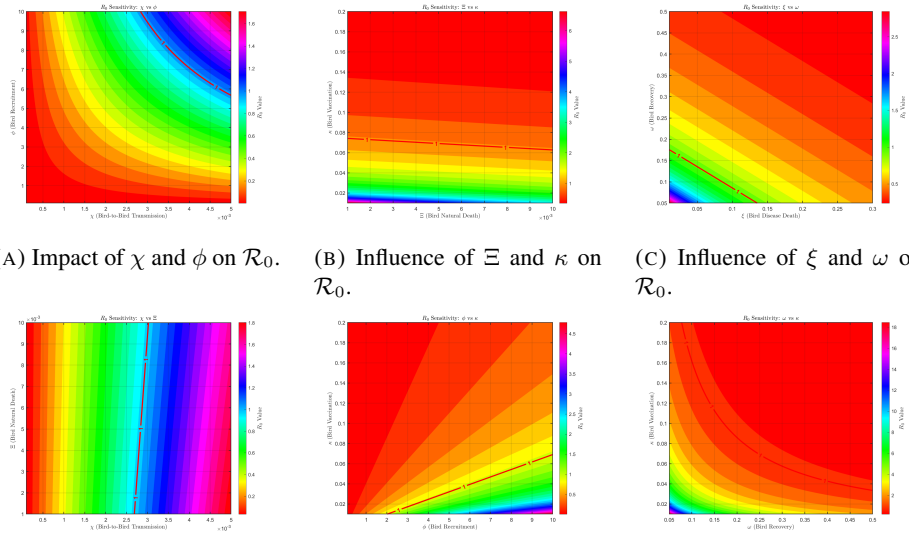

(A) Impact of χ and ϕ on $\mathcal{R}_0$.

(B) Influence of Ξ and κ on $\mathcal{R}_0$.

(C) Influence of ξ and ω on $\mathcal{R}_0$.

(D) Influence of χ and Ξ on $\mathcal{R}_0$.

(E) Influence of ϕ and κ on $\mathcal{R}_0$.

(F) Influence of parameters ω and κ on $\mathcal{R}_0$.

FIGURE 3. Impact of various parameters on $\mathcal{R}_0$ through 2D contour plots.

4.10. **Global sensitivity analysis.** We perform a global sensitivity analysis of the disease outcomes with Latin hypercube sampling (LHS) and partial rank correlation coefficients (PRCC) to quantify the impact of the model parameters on the disease outcome. Such an approach is commonly employed in epidemiological modelling to determine the parameters that mainly influence the dynamics of the system, taking into account interactions between parameters and their nonlinearity. The analysis is performed with $N = 500$ samples from the LHS that were selected within biologically feasible ranges of the parameters listed in Table 4. The values of PRCCs are obtained by deflating both the input and output, followed by the calculation of partial correlations between each of the parameters and the output, setting the rest of the parameters at the rank values. The criteria for statistical significance are performed by Fisher's z-transformation, and $p < 0.05$ is considered significant.

Figure 4a presents the PRCC bar plots showing the influence of parameters on peak human infection, peak bird infection, total human cases, and bird reproductive number. The parameters influencing the peak of human infections are those influencing bird-to-bird transmission and bird recovery. The key parameters for the birds, including recruitment, transmission, and recovery, control the infected birds. The total human cases are also affected by bird parameters and the vaccination (υ). The reproductive number for birds is

effected by transmission (χ), recruitment (ϕ), natural mortality (Ξ), and recovery (ω). In terms of policy implications, the bird transmission parameters are always dominant in all outputs indicating that interventions focusing on the bird population have the highest impact on human health. The important negative effect of human vaccination on all human outputs suggests a vaccination program for high-risk groups such as poultry workers and health workers. Most bird parameters are statistically significant, giving good quantitative proof to support efforts to allocate resources to avian influenza surveillance and control programs. Figure 4b provides the ranking of all parameters on infected humans. Green bars represent positive correlation, red bars represent negative correlation. The bird-to-bird transmission rate has the most important influence and is highly positively correlated with human cases. The second most relevant parameter was bird recovery, with a negative correlation, suggesting that a quicker recovery in birds leads to a shorter infectious period and less exposure for humans. Human infection is positively related to bird recruitment, with a greater number of susceptible birds maintaining the transmission. The bird-to-human transmission (β) has a positive correlation. The most influential human side parameter is human vaccination, which has a strong negative correlation, indicating its protective effect. Figure 4c presents the PRCC heatmap showing the sensitivity of four outputs to all parameters. Red indicates positive correlation, blue indicates negative correlation. Values closer to ± 1 indicate stronger influence. The heatmap offers an overall prioritization scheme for intervention strategies, with bird transmission and recruitment (ϕ) being the most effective strategies to reduce all measures of infection. A strong negative correlation between human vaccination across human outputs provides justification for dual policy approaches of controlling the bird reservoir while vaccinating high-risk human populations.

Figure 4d displays the scatter plots reflecting the influence of bird-to-bird transmission, bird recovery, bird recruitment and human vaccination on peak human infection. Positive correlation between bird-to-bird transmission (χ) and peak human infection suggests that transmission rate is the greatest human health risk. The relationship between bird recovery and infection is highly negative, suggesting that the shorter the infectious period, the sooner birds recover and the less spread. The positive relationship between infection and bird recruitment shows that the number of infected birds increases with the number of birds recruited. The high level of a negative correlation between human vaccination and infection demonstrates the protective benefit of a person being vaccinated. The bird-to-bird transmission (χ) is the highly influential parameter, recommending high priority intervention through the reduction of contact rates through biosecurity, reduced stocking density, and movement restrictions. A negative correlation (ω) indicates that the quality of supportive veterinary care and early detection may shorten the infectiousness period in poultry. The impact of bird recruitment (ϕ) emphasizes the need for poultry population management such as decreasing flock size and managing for depopulation during outbreaks. Vaccination of humans (υ) possesses a protective effect and represents strong evidence for the implementation of prophylactic vaccination programs for poultry workers and healthcare providers.

4.11. **Statistical analysis.** In this part, we perform the statistical analysis for all compartments of the avian influenza model. High standard deviation, range, and coefficient of

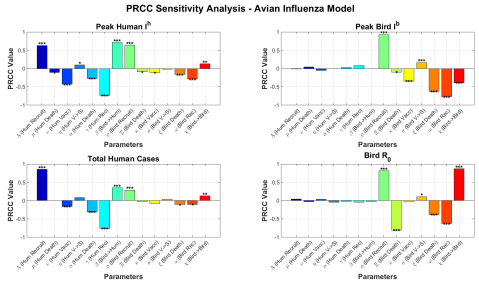

(A) PRCC bar plots showing the sensitivity of parameters.

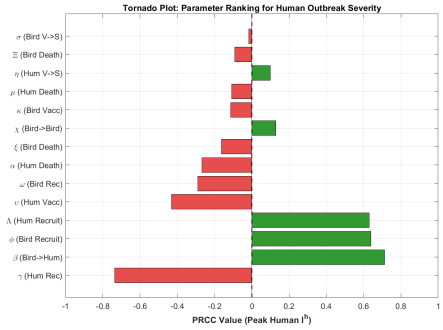

(B) Tornado plot ranking the influence of parameters on peak human infection.

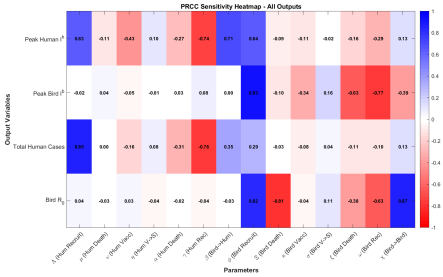

(C) PRCC heatmap showing the sensitivity of four outputs to all parameters.

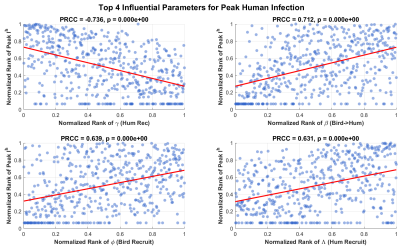

(D) Scatter plots of the top 4 influential parameters vs peak human infection.

FIGURE 4. Global sensitivity analysis plots showing the impact of various parameters on $\mathcal{R}_0$.

variation reflect slower convergence, and larger temporal fluctuations, while small dispersion values exhibit quick stability and lower variation. Higher standard deviation, range and coefficient of variation indicate greater variability. The coefficient of variation is used as the main parameter to measure relative dispersion. The skewness and kurtosis measure the degree of asymmetry and peakedness of the compartment distribution. Positive skewness indicates occasional persistence of higher population values, while negative skewness reflects a tendency toward lower values. Kurtosis values greater than three suggest heavy-tailed distributions and increased sensitivity to extreme fluctuations, while values below three indicate a more uniform distribution around the mean. Most compartments are nearly symmetric. Values of kurtosis below three indicate platykurtic distributions, while values above three indicate leptokurtic distributions. All compartments exhibit platykurtic behaviour. Strong positive correlations are observed between infected and recovered humans, and for birds, between susceptible and vaccinated birds. Negative correlations appear between susceptible and infected, reflecting the expected epidemiological relationship. Figure 5a presents the box plots of steady-state distributions for all compartments. The central mark indicates the median, box edges represent the 25th and 75th percentiles, and whiskers extend to the most extreme data points. Outliers are shown as individual points. Figure 5b illustrates the mean values with 95% confidence intervals for all compartments at steady state. Error bars represent the standard error of the mean. The intervals reflect the precision of the estimated equilibrium populations. Figure 5c displays histograms of steady-state population values for all compartments. The distributions are approximately unimodal and symmetric for most compartments, with narrow spreads for susceptible birds and wider spreads for recovered birds. Figure 5d depicts notched box plots showing medians with 95% confidence intervals of the medians. Overlapping notches indicate that medians are not significantly different. Most compartments show distinct median values, confirming their epidemiological separation.

4.12. **Chaos test.** Chaos theory has transformed our comprehension of complicated dynamical systems, including epidemiological models. Even with correct model formulation and parameter knowledge, chaotic behavior in disease systems suggests that long-term prediction is limited. Chaos results from sensitive dependency on initial conditions. Determining if disease dynamics are chaotic is essential for determining how predictable epidemics are, creating efficient early warning systems, assessing the validity of deterministic models, and developing adaptive intervention tactics.

In this section, we aim to measure chaotic behavior in the compartments of the model using the 0-1 test, compare the intensity of chaos in all compartments, determine which parts of the system are the most and least chaotic, offer biological explanations for chaos in each compartment, and discuss the implications of disease dynamics for public health. The 0-1 chaos test is a binary test that differentiates between chaotic and regular dynamics in deterministic systems. The 0-1 test is computationally efficient and does not require phase space reconstruction, as compared to the Lyapunov exponent approach.

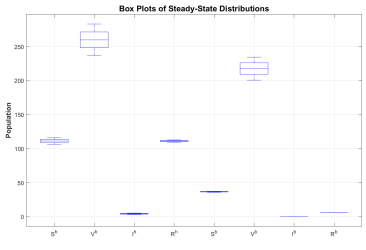

(A) Box plots of steady-state distributions for all compartments.

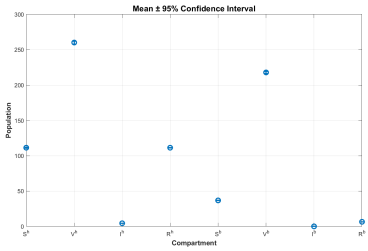

(B) Mean values with 95% confidence intervals for each compartment at steady state.

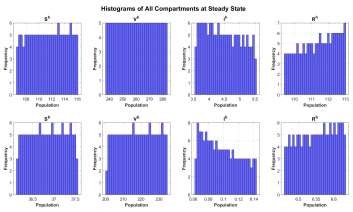

(C) Histograms of steady-state population values for all eight compartments.

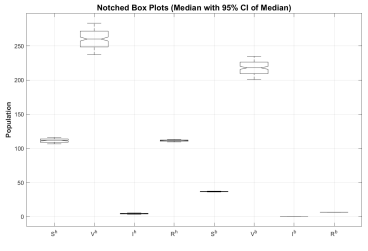

(D) Notched box plots showing medians with 95% confidence intervals of the medians.

FIGURE 5. Statistical analysis of the compartments of the model.

Let $\phi(n)$ be a time series of length N. The test proceeds as follows: For a chosen $c \in (0, \pi)$, define translation variables:

$$p_c(n) = \sum_{j=1}^{n} \phi(j) \cos(jc), \quad n = 1, 2, \ldots, N, q_c(n) = \sum_{j=1}^{n} \phi(j) \sin(jc), \quad n = 1, 2, \ldots, N.$$

Define the mean square displacement as:

$$M_c(n) = \lim_{N \to \infty} \frac{1}{N} \sum_{j=1}^{N} \left[(p_c(j+n) - p_c(j))^2 + (q_c(j+n) - q_c(j))^2 \right].$$

For finite N, we compute:

$$M_c(n) = \frac{1}{N-n} \sum_{j=1}^{N-n} \left[(p_c(j+n) - p_c(j))^2 + (q_c(j+n) - q_c(j))^2 \right].$$

For regular dynamics, $M_c(n)$ remains bounded. For chaotic dynamics, $M_c(n)$ grows linearly with n:

$$M_c(n) \sim D_c n \quad \text{as } n \to \infty.$$

The asymptotic growth rate K_c is computed via correlation:

$$K_c = \text{corr}(\xi, \Delta),$$

where $\xi = (1, 2, \ldots, n_{\max})$ and $\Delta = (M_c(1), M_c(2), \ldots, M_c(n_{\max}))$. To eliminate dependence on c, we take the median over multiple c values:

$$K = \text{median}(K_{c_1}, K_{c_2}, \ldots, K_{c_m}),$$

where c_j are chosen from $(0, \pi)$. **Theorem 8:** For a regular dynamical system, $K = 0$. For

TABLE 5. Classification of dynamics based on K Value.

K value range	Classification	Dynamical behavior
$K < 0.2$	Regular	Periodic or stable equilibrium
$0.2 \leq K < 0.5$	Weak Chaos	Intermittent chaotic bursts.
$0.5 \leq K < 0.8$	Moderate Chaos	Mixed regular-chaotic dynamics.
$K \geq 0.8$	Strong Chaos	Fully developed deterministic chaos.

a chaotic system, $K = 1$.

Proof: For regular dynamics, $p_c(n)$ and $q_c(n)$ are bounded functions, leading to bounded $M_c(n)$ and thus $K = 0$. For chaotic dynamics, $p_c(n)$ and $q_c(n)$ behave like Brownian motion, yielding linear growth of $M_c(n)$ and $K = 1$.

The test is implemented with c values: $\pi/5, \pi/4, \pi/3, \pi/2, 2\pi/3$, $n_{\max} = N/10$ (where N is time series length), median of K_c values for robustness.

The bar chart in Figure 6a displays the results of the 0-1 chaos test for all compartments. The chaos statistic K for each compartment is shown in this plot as a vertical bar chart. Classification thresholds at K = 0.2 show the presence of regular or weak chaos, K = 0.5 shows the presence of a weak or moderate chaos boundary, and K = 0.8 shows moderate or strong chaos, shown by horizontal dashed lines. Figure 6b shows a line plot reflecting chaos values for compartments with threshold lines. Figure 6c presents the P-Q plots for all compartments. Bounded trajectories are produced by regular dynamics for every compartment. The scatter plot in Figure 6d displays the intensity of chaos using a color gradient. Each compartment's K value is shown in this scatter plot, with color intensity denoting the degree of disorder. Each point has a numerical designation above it. Biologically, all compartments show regular, predictable dynamics.

4.13. **Phase plots.** In this section, we provide the phase plots to show the interaction of the compartments. Figure 7a shows the interaction between susceptible and infected birds. As susceptibility declines, infected birds quickly surge to an early peak before rapidly declining as a result of vaccination and recovery processes. As the system stabilizes, the parabolic arc exhibits efficient infection control. Figure 7b shows the relationship between susceptible and recovered birds. Recovered birds grow in a sigmoidal pattern, peaking during infection and then declining. The curve demonstrates immune saturation, with susceptible birds stabilizing and recovered birds approaching maximum levels. Figure 7c describes the relationship between susceptible and vaccinated birds. The susceptible birds sharply fall, while vaccinated birds increase quickly. As vaccination reaches complete protection, declining immunity results in a steady increase in susceptibility while vaccination rates stabilize. Figure 7d presents the interactions between vaccinated and infected birds. Despite vaccination, the infected birds rise initially before peaking and falling abruptly as vaccine

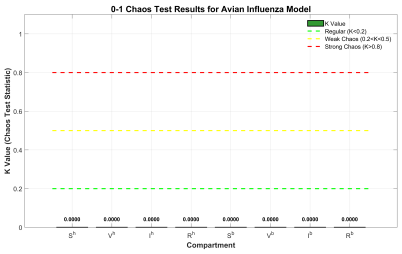

(A) Plot showing the K values of all compartments through a vertical bar chart.

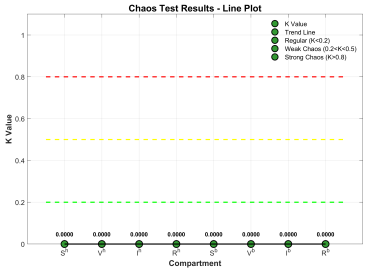

(B) Line plot showing K values for all compartments.

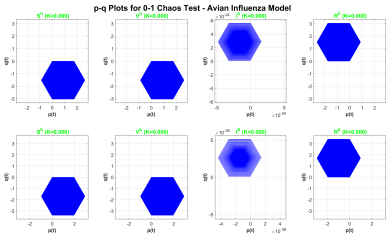

(C) Figure showing pq plots for all compartments.

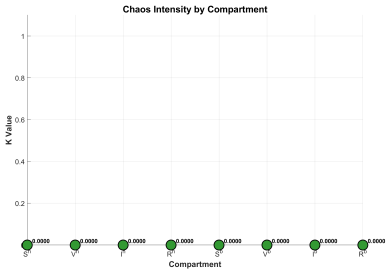

(D) Scatter plot showing chaos intensity for all compartments.

FIGURE 6. Figures showing that the behaviour of the compartments is bounded and the system does not exhibit chaos.

coverage increases. Three control phases are revealed by the pattern: near-elimination, effective containment, and starting spread. Figure 7e shows the relationship between susceptible and infected humans. As the susceptible humans decline, the infected humans increase exponentially, reaching a clear epidemic peak. After the peak, infections gradually decrease as a result of immunity building and treatments, and susceptible humans level out at lower levels. Figure 7f describes the relationship between susceptible and recovered humans. Recovered humans quickly rise during periods of high infection, then fluctuate as transient immunity declines. The trajectory spirals in the direction of equilibrium, where susceptible humans keep a fixed proportion and recovered humans remain stable. Figure 7g shows the interaction of susceptible and vaccinated humans. The vaccinated humans first increase, while susceptible humans drastically decrease as vaccination increases. Susceptible humans gradually recover over time when vaccination rates stabilize and approach equilibrium due to declining immunity. Figure 7h shows the interaction between vaccinated and infected humans. Human infections sharply fall when vaccination rates rise, and then continue to decline as coverage is increased. The vaccinated humans exhibit distinctive L-shaped short-term defense that develops into long-term herd immunity.

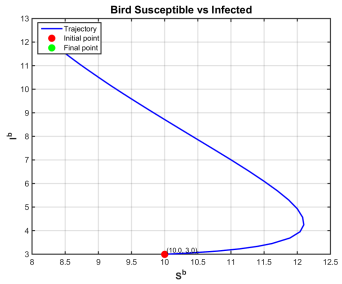

(A) Interaction of sensitive VS infected birds.

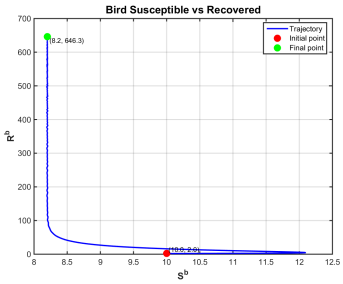

(B) Interaction of sensitive VS recovered birds.

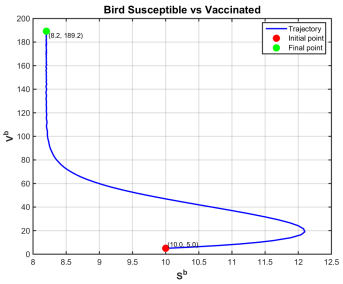

(C) Interaction of sensitive VS vaccinated birds.

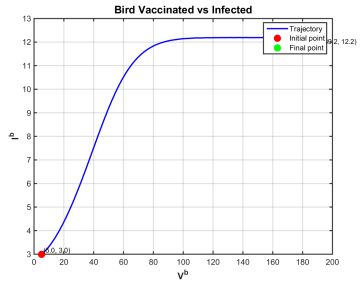

(D) Interactions of vaccinated VS infected birds.

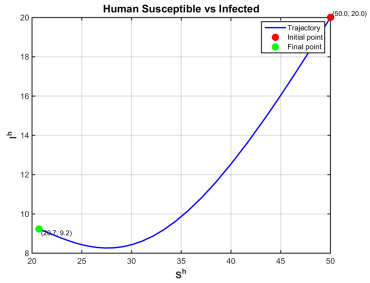

(E) Interaction of sensitive and vaccinated humans.

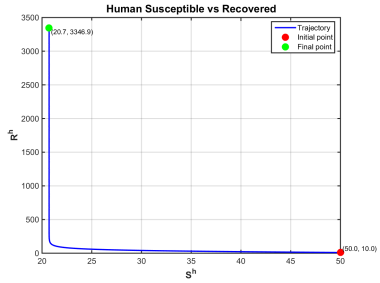

(F) Interaction of sensitive VS recovered humans.

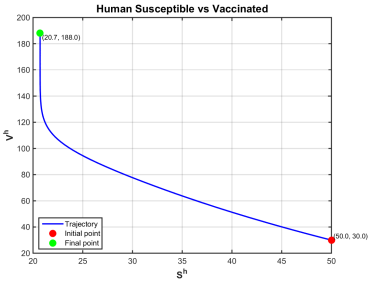

(G) Interaction of sensitive VS vaccinated humans.

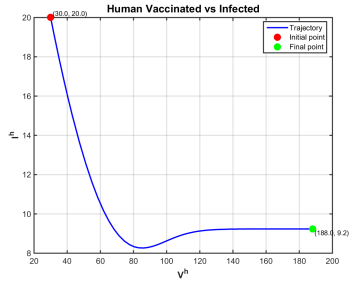

(H) Interaction of vaccinated and infected humans.

FIGURE 7. Interaction of various human and bird groups through 2D phase plots.

5. TRANSCRITICAL BIFURCATION ANALYSIS

The transcritical bifurcation in this avian influenza model represents a phenomenon that controls the disease shift between elimination and persistence. When $\mathcal{R}_0 < 1$, the system shows disease-free stability where small outbreaks vanish, while $\mathcal{R}_0 > 1$ induces a shift enabling persistence of disease. This bifurcation analysis is essential for epidemiology as it determines exact disease eradication conditions, assesses the impact of control measures on the epidemic threshold, and shows the lack of cyclic effects that could make disease control more difficult. We analyze the bifurcation behavior of the system at the critical threshold $\mathcal{R}_0 = 1$ using the Castillo-Chavez and Song bifurcation theorem [16]. This analysis reveals the nature of the bifurcation and provides insight into the disease dynamics.

We select the bird-to-bird transmission rate χ as the bifurcation parameter. At the critical value:

$$\chi^* = \frac{\Xi(\kappa + \Xi + \sigma)(\xi + \Xi + \omega)}{\phi(\Xi + \sigma)},$$

such that $\mathcal{R}_0 = 1$ when $\chi = \chi^*$.

Consider the system:

$$\frac{d\mathbf{x}}{dt} = \mathbf{f}(\mathbf{x}, \chi), \quad \mathbf{f} : \mathbb{R}^8 \times \mathbb{R} \to \mathbb{R}^8,$$

where χ is the bifurcation parameter. At $\chi = \chi^*$, the system has a disease-free equilibrium $\mathbf{x} = \mathbf{0}$ and the Jacobian matrix $J = D_{\mathbf{x}}\mathbf{f}(\mathbf{0}, \chi^*)$ has a simple zero eigenvalue.

Let $\mathbf{w} = (w_1, w_2, \ldots, w_8)^T$ be the right eigenvector corresponding to the zero eigenvalue, satisfying $J\mathbf{w} = 0$. From the Jacobian structure at $\chi = \chi^*$, choosing $w_7 = 1$, we obtain:

$$\mathbf{w} = \big(-\frac{\beta S_0^h(\eta + \mu)}{\mu(\eta + \mu + \upsilon)}, \frac{\upsilon}{\eta + \mu} w_1, \frac{\beta S_0^h}{\alpha + \mu + \gamma}, \frac{\gamma\beta S_0^h}{\mu(\alpha + \mu + \gamma)}, -\frac{\chi^* S_0^b(\Xi + \sigma)}{\Xi(\kappa + \Xi + \sigma)}, \frac{\kappa}{\Xi + \sigma} w_5, 1, \frac{\omega}{\Xi} \big)^T.$$

Let $\mathbf{v} = (v_1, v_2, \ldots, v_8)$ be the left eigenvector satisfying $\mathbf{v}J = \mathbf{0}$ and $\mathbf{v} \cdot \mathbf{w} = 1$ given by:

$$\mathbf{v} = (0, 0, 0, 0, 0, 0, 1, 0),$$

with normalization $\mathbf{v} \cdot \mathbf{w} = 1$ satisfied since $w_7 = 1$.

The bifurcation coefficients are defined as:

$$a = \sum_{k,i,j=1}^{n} v_k w_i w_j \frac{\partial^2 f_k}{\partial x_i \partial x_j}(0, \chi^*), b = \sum_{k,i=1}^{n} v_k w_i \frac{\partial^2 f_k}{\partial x_i \partial \chi}(0, \chi^*).$$

First, we compute the coefficient a. Since $v_k = 0$ for all $k \neq 7$, only the $k = 7$ term contributes. The infected bird equation f_7 is:

$$f_7 = \chi S^b I^b - (\xi + \Xi + \omega) I^b.$$

The non-zero second derivatives are:

$$\frac{\partial^2 f_7}{\partial S^b \partial I^b} = \chi, \quad \frac{\partial^2 f_7}{\partial I^b \partial S^b} = \chi.$$

Therefore:

$$\begin{aligned} a &= v_7 \left[w_5 w_7 \frac{\partial^2 f_7}{\partial S^b \partial I^b} + w_7 w_5 \frac{\partial^2 f_7}{\partial I^b \partial S^b} \right] \\ &= 1 \cdot 2\chi^* w_5 w_7. \end{aligned}$$

Substituting $w_5 = -\dfrac{\chi^* {S^b}^0 (\Xi + \sigma)}{\Xi(\kappa + \Xi + \sigma)}$ and $w_7 = 1$, the expression for a becomes:

$$a = -\frac{2(\chi^*)^2 {S^b}^0 (\Xi + \sigma)}{\Xi(\kappa + \Xi + \sigma)}.$$

Since all parameters are positive, $\boldsymbol{a < 0}$.

Now, we compute the coefficient b. Again, only $k = 7$ contributes. The non-zero second derivative with respect to χ:

$$\frac{\partial^2 f_7}{\partial I^b \partial \chi} = {S^b}^0.$$

Therefore:

$$b = v_7 w_7 \frac{\partial^2 f_7}{\partial I^b \partial \chi} = 1 \cdot 1 \cdot {S^b}^0 = {S^b}^0 > 0.$$

Since $a < 0$ and $b > 0$, the system exhibits a forward transcritical bifurcation.

At transmission rate $\chi = \chi^*$. For transmission rate χ less than a particular value χ^*, the reproductive number $\mathcal{R}_0 < 1$ and so the Influenza-free equilibrium point is stable, and no endemic equilibrium exists. For transmission rateχ larger than its critical value χ^*, reproductive number $\mathcal{R}_0$ becomes larger than unity and the Influenza-free equilibrium point is unstable and a stable endemic equilibrium emerges. The endemic equilibrium appears from the Influenza-free equilibrium point as $\mathcal{R}_0$ exceeds 1. There is no backward bifurcation, so disease eradicates when $\mathcal{R}_0 < 1$. Reducing $\mathcal{R}_0$ below 1 is sufficient for disease elimination without requiring additional control efforts. The bifurcation is independent of the fractal-fractional parameters, which only affect the transient dynamics and convergence rates.

Figure 8 displays the bifurcation diagram showing how the bifurcation parameter χ affects the infected humans and birds. The impact of the transmission rate on the influenza-persistent equilibrium with dependence on the initial population of birds indicates faster endemicity at increasing rates of transmission. The bifurcation study of the Avian Influenza model in χ–κ space reveals stability regions that are indicated by $\mathcal{R}_0 = 1$. The red zone indicates influenza persistence, while the green region shows a disease-free equilibrium when $\mathcal{R}_0 < 1$ that can be obtained with vaccination. The connection between vaccination and transmission rate is shown by the critical threshold curve, which demonstrates that higher κ can maintain stability even at higher transmission rates. In Figure 9, for $\mathcal{R}_0 < 1$, the solid blue curve represents a stable disease-free equilibrium; for $\mathcal{R}_0 > 1$, the dotted blue curve represents an unstable Influenza-free equilibrium point. Stable endemic equilibrium is shown by the red curve as it is beyond the critical threshold. The plot shows how the endemic equilibrium of infected birds ${I^b}^*$ is controlled by changes in the bird-to-bird transmission rate. Disease elimination is ensured by the disease-free equilibrium ${I^b}^* = 0$ remaining stable below the threshold χ^*. This threshold behavior is visually shown by a vertical line at $\chi = \chi^*$, where $\mathcal{R}_0 < 1$ indicates eradication and $\mathcal{R}_0 > 1$ indicates endemic

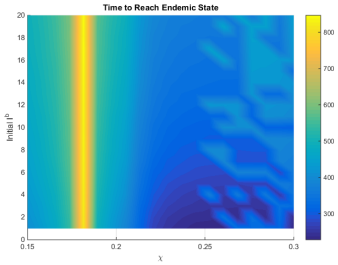

(A) Plot showing the impact of transmission rate on the endemic equilibrium points.

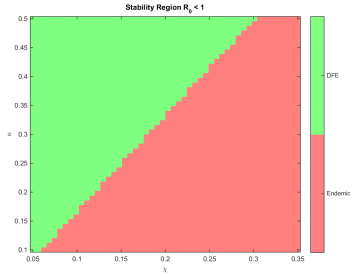

(B) χ–κ Contour plot illustrating stability regions indicated by $\mathcal{R}_0 = 1$.

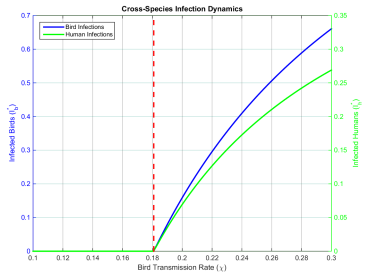

(C) Plot illustrates how transmission rate spreads disease in humans and birds.

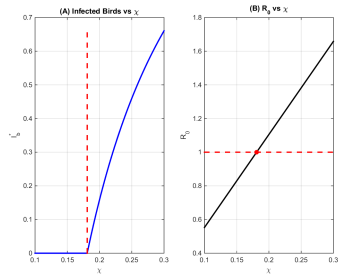

(D) An illustration of how transmission rate χ increases the number of infected birds and $\mathcal{R}_0$.

FIGURE 8. Bifurcation diagrams showing how the bifurcation parameter χ affects the infected humans and birds.

persistence. Rising Avian transmission also increases human infections. Stability region of parameters χ, κ demonstrate that greater bird vaccination rates κ also increase the critical χ^* threshold, thus helps us to control disease irrespective of increased transmission. Figure 10 uses the basic reproduction number $\mathcal{R}_0$ to define three different epidemiological regimes. The disease-free equilibrium is both locally and globally asymptotically stable in the subcritical regime ($\mathcal{R}_0 < 1$). This means that small introductions of infected birds decay exponentially, and disease elimination is still possible through control measures. Influenza-free and existing equilibrium points coincide during the stability transition at the critical threshold ($\mathcal{R}_0 = 1$), indicating the exact elimination boundary where the spread of disease either decreases or the disease is eliminated. With explicit predominance formulations $I^{b^\star}$, influenza persistent equilibrium points become locally stable in the supercritical zone ($\mathcal{R}_0 > 1$). The influenza-free equilibrium becomes unstable, resulting in an endemic durability in which $\mathcal{R}_0$ represents a monotonic rise in disease prevalence.

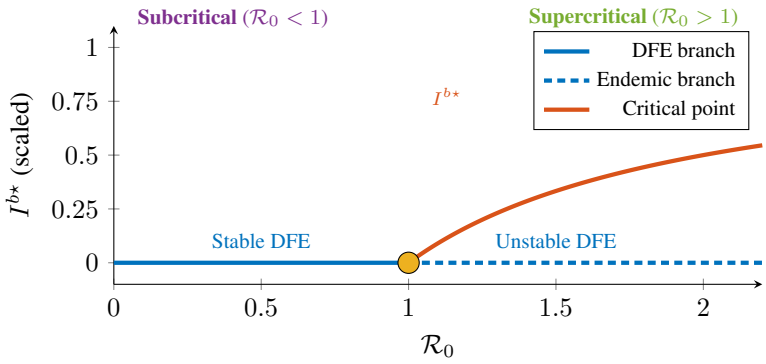

FIGURE 9. Plot showing the transition of equilibrium points as the reproductive number varies.

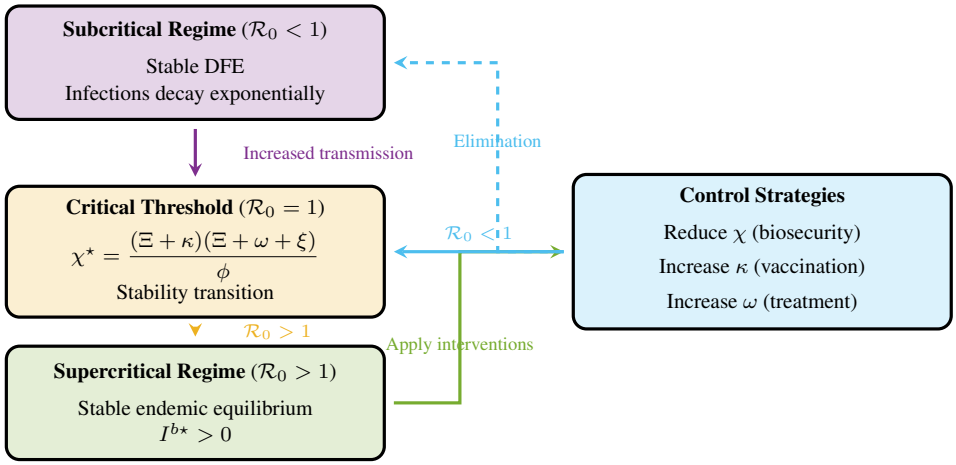

FIGURE 10. Figure showing the dynamic shifts across the threshold of an epidemic.

6. NUMERICAL SCHEME BASED ON NEWTON POLYNOMIALS

In this part, we provide a numerical approach for the fractal–fractional model (3.4) based on Newton polynomials, as studied in [12]. The numerical simulation of infectious disease models has made extensive use of this method due to its accuracy and efficiency. Several studies [23] showed that Newton polynomial-based techniques are more accurate and reliable than the traditional Adams–Bashforth method, which uses Lagrange polynomial interpolation. The scheme converges unconditionally for all step sizes and convergence order $\mathcal{O}(\Delta t)^{\rho\zeta+1}$, while the Adams-Bashforth method in contrast is only conditionally stable. The Newton polynomial method has a higher order of convergence, errors about one to

two orders of magnitude lower, naturally includes memory effects, and is computationally efficient with $\mathcal{O}(N^2)$.

Applying fractal-fractional integral (2.2) to the system (3.4) and incorporating the Newton polynomial approximation yields the following discrete representation:

$$
\begin{aligned}
(S^{\hbar})^{k+1} = S^{\hbar}(0) &+ \frac{(1-\rho)\zeta}{A\text{ß}(\rho)} t_k^{\zeta-1} S_1^{\hbar}\left(t_k, \beth\right) + \frac{(\rho)\zeta(\Delta t)^{\rho}}{A\text{ß}(\rho)\Gamma(\rho+1)} \sum_{j=2}^{k} S_1^{\hbar}\left(t_{j-2}, \varpi\right) \\
& t_{j-2}^{\zeta-1} \times [(k-j+1)^{\rho} - (k-j)^{\rho}] + \frac{\rho\zeta(\Delta t)^{\rho}}{A\text{ß}(\rho)\Gamma(\rho+2)} \\
& \sum_{j=2}^{k} \frac{1}{\Delta t} \Big[t_{j-1}^{\zeta-1}, (S_1^{\hbar})\left(t_{j-1}, \beth\right) - t_{j-2}^{\zeta-1}(S_1^{\hbar})\left(t_{j-2}, \varpi\right) \Big] \\
& \times [(k-j+1)^{\rho} \times (k-j+3+2\rho) - (k-j)^{\rho}(k-j+3+3\rho)] \\
& + \frac{\rho\zeta}{A\text{ß}(\rho)\Gamma(\rho)} \sum_{j=2}^{k} \frac{1}{2\Delta t^2} \Big[t_j^{\zeta-1}(S_1^{\hbar})\left(t_j, \aleph\right) - 2t_{j-1}^{\zeta-1}(S_1^{\hbar})\Big(t_{j-1}, \beth\Big) \\
& + t_{j-2}^{\zeta-1}(S_1^{\hbar})\Big(t_{j-2}, \varpi\Big)\Big] \\
& \times \Big[(k-j+1)^{\rho}\left\{2(k-j)^2 + (3j+10)(k-j) + 2j^2 + 9j + 12\right\} \\
& - (k-j)^{\rho}\left\{2(k-j)^2 + (5\rho+10) + (6\rho^2+18\rho+12)\right\}\Big],
\end{aligned}
$$

where

$$
\begin{aligned}
\aleph &= (S^{\hbar})^j, (V^{\hbar})^j, (I^{\hbar})^j, (R^{\hbar})^j, (S^b)^j, (V^b)^j, (I^b)^j, (R^b)^j, \\
\beth &= (S^{\hbar})^{j-1}, (V^{\hbar})^{j-1}, (I^{\hbar})^{j-1}, (R^{\hbar})^{j-1}, (S^b)^{j-1}, (V^b)^{j-1}, (I^b)^{j-1}, (R^b)^{j-1}, \\
\varpi &= (S^{\hbar})^{j-2}, (V^{\hbar})^{j-2}, (I^{\hbar})^{j-2}, (R^{\hbar})^{j-2}, (S^b)^{j-2}, (V^b)^{j-2}, (I^b)^{j-2}, (R^b)^{j-2}, \\
\beth &= S^{\hbar}(t_k), V^{\hbar}(t_k), I^{\hbar}(t_k), R^{\hbar}(t_k), S^b(t_k), V^b(t_k), I^b(t_k), R^b(t_k).
\end{aligned}
$$

This establishes the numerical procedure for the susceptible humans class, following the analogous procedure, the scheme for other compartments can be derived.

6.1. **Convergence and stability of the scheme.** In this part, we include a convergence and stability analysis of the Newton polynomial numerical scheme for our fractal-fractional system.

The numerical scheme based on Newton polynomials used to solve the fractal-fractional order system is given by:

$$
y(t_{n+1}) = y(t_n) + \frac{(\Delta t)^{\rho\zeta}}{\Gamma(\rho+1)} \sum_{j=0}^{n} \left[\frac{(n-j+1)^{\rho} - (n-j)^{\rho}}{(\rho+1)} \right] f(t_j, y(t_j)) + \mathcal{R}_n.
$$

where $\mathcal{R}_n$ is the remainder term from the Newton interpolation.

Theorem 9: Let $f(t, y)$ be Lipschitz continuous in y with Lipschitz constant $L > 0$, and let $y(t)$ be the exact solution of the fractal-fractional system. Then the Newton polynomial

scheme converges with order $\mathcal{O}(\Delta t)^{\rho\zeta+1}$, i.e.:

$$\max_{0\leq n\leq N} \|y_n - y(t_n)\| \leq C(\Delta t)^{\rho\zeta+1},$$

where C is a positive constant independent of the step size Δt.

Proof: The local truncation error of the Newton polynomial scheme is:

$$E_{n+1} = y(t_{n+1}) - y(t_n) - \frac{(\Delta t)^{\rho\zeta}}{\Gamma(\rho+1)} \sum_{j=0}^{n} \left[\frac{(n-j+1)^{\rho} - (n-j)^{\rho}}{(\rho+1)} \right] f(t_j, y(t_j)).$$

Using the Taylor expansion of the exact solution around t_n:

$$y(t_{n+1}) = y(t_n) + \frac{(\Delta t)^{\rho\zeta}}{\Gamma(\rho+1)} \sum_{j=0}^{n} \left[\frac{(n-j+1)^{\rho} - (n-j)^{\rho}}{(\rho+1)} \right] f(t_j, y(t_j)) + \mathcal{O}(\Delta t)^{\rho\zeta+2}.$$

Therefore, the local truncation error satisfies:

$$\|E_{n+1}\| \leq C_1(\Delta t)^{\rho\zeta+2}.$$

The global error propagation satisfies:

$$e_{n+1} = e_n + C_2\Delta t \cdot e_n + C_1(\Delta t)^{\rho\zeta+2}.$$

Summing over $n = 0, \ldots, N-1$:

$$\|e_N\| \leq C_1(\Delta t)^{\rho\zeta+1} \frac{e^{C_2 T} - 1}{C_2}.$$

Thus:

$$\max_{0\leq n\leq N} \|e_n\| \leq C(\Delta t)^{\rho\zeta+1}.$$

This proves the convergence of the scheme.

6.2. **Stability analysis.** A numerical scheme is stable if small perturbations in the initial conditions do not cause large changes in the numerical solution.

Theorem 10: The Newton polynomial scheme for the fractal-fractional system is unconditionally stable for all $\rho \in (0, 1]$, $\zeta \in (0, 1]$, and $\Delta t > 0$.

Proof: Consider two numerical solutions y_n and $\tilde{y}_n$ with perturbed initial conditions y_0 and $\tilde{y}_0$. Define the error $e_n = y_n - \tilde{y}_n$.

The error dynamics satisfy:

$$e_{n+1} = e_n + \frac{(\Delta t)^{\rho\zeta}}{\Gamma(\rho+1)} \sum_{j=0}^{n} \left[\frac{(n-j+1)^{\rho} - (n-j)^{\rho}}{(\rho+1)} \right] [f(t_j, y_j) - f(t_j, \tilde{y}_j)].$$

Using the Lipschitz condition:

$$\|f(t_j, y_j) - f(t_j, \tilde{y}_j)\| \leq L\|e_j\|.$$

Therefore:

$$\|e_{n+1}\| \leq \|e_n\| + \frac{(\Delta t)^{\rho\zeta} L}{\Gamma(\rho+1)} \sum_{j=0}^{n} \left[\frac{(n-j+1)^{\rho} - (n-j)^{\rho}}{(\rho+1)} \right] \|e_j\|.$$

By the Gronwall inequality for discrete fractional systems:

$$\|e_n\| \leq \|e_0\| \mathcal{E}_\rho \left(\frac{L(\Delta t)^{\rho\zeta}}{\Gamma(\rho+1)} n^\rho \right).$$

where $\mathcal{E}_\rho$ is the Mittag-Leffler function.

Figure 11 compares the infected population trajectory of the humans and birds at various time step sizes. The solutions are approaching the reference solution as the step size gets smaller, which shows the consistency of the Newton polynomial scheme. The similar solution for $\Delta t = 0.02$ with the reference solution confirms the accuracy for small step sizes. This validation is important to guarantee the reliability of the numerical simulations. The Newton polynomial solver for FFM is analysed for convergence in Table 6. The L_1 error, L_2 error, and L_∞ error all decrease as the time step size becomes smaller, which is evidence of convergence of the scheme. The order of convergence of the Newton polynomial scheme is close to the theoretical order, which shows the accuracy of the scheme. The CPU time rises as step size decreases, as more accurate calculations come at a high cost. This Table offers quantitative evidence of the reliability of the scheme in simulations of the Avian Influenza fractal-fractional model. The stability analysis of the Newton polynomial solver is summarized in Table 7. All compartments checked for positivity and boundedness. Numerical outcomes indicate conditional stability. The infected humans and the infected birds at the peak and at the end of the epidemic are shown to be independent of the number of time steps, suggesting the scheme is stable. The results indicate that the solver returns stable solutions for all step sizes tested and, thus, is robust for long-time simulations. This stability is essential for a proper representation of the long-term dynamics of the transmission of avian influenza. A summary of the experimental order of convergence (EOC) for the Newton polynomial solver is given in Table 8. The mean EOC values for L_1, L_2, and L_∞ errors are the same and have the theoretical order of $\mathcal{O}(\Delta t)$, further validating the convergence of the scheme. The standard deviations show the uniformity of convergence with the various step sizes. This table provides a validation of the theoretical convergence property of the Newton polynomial scheme.

TABLE 6. Convergence analysis of the Newton polynomial scheme showing error norms and experimental order of convergence (EOC).

Step size Δt	L_1 **Error**	L_2 **Error**	L_∞ **Error**	**EOC** (L_2)	**CPU Time (s)**
0.5000	6.38e+00	7.27e+00	1.15e+01	0.1251	0.00
0.2500	5.89e+00	6.66e+00	1.05e+01	0.2056	0.00
0.1000	5.13e+00	5.78e+00	9.03e+00	0.1957	0.00
0.0500	4.50e+00	5.05e+00	7.84e+00	0.2436	0.00
0.0250	3.81e+00	4.26e+00	6.59e+00	0.4356	0.01
0.0100	2.82e+00	3.15e+00	4.84e+00	–	0.02

7. NUMERICAL SIMULATION

We evaluate the impact of our findings using fractal fractional operator analysis, disease spread analysis, and robust numerical techniques. Extraordinary outcomes can be obtained

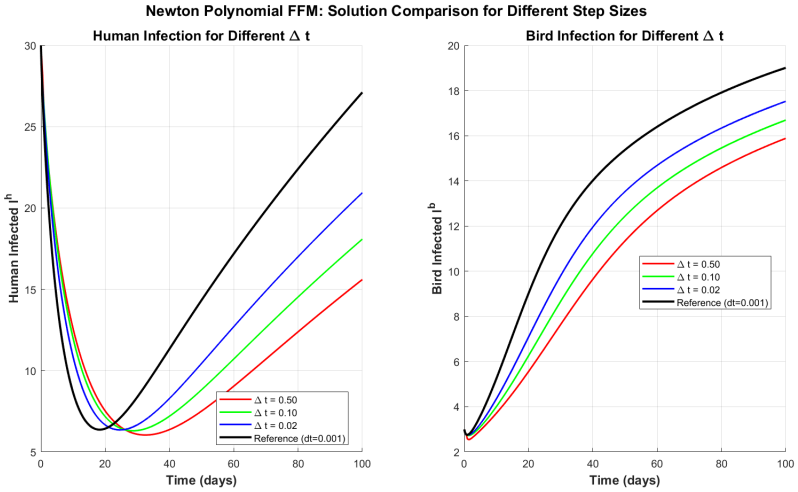

FIGURE 11. Comparison of human and bird infected populations for different step sizes using the Newton polynomial scheme.

TABLE 7. Stability analysis of the Newton polynomial FFM solver showing peak and final infected populations for different time step sizes.

Step Size Δt	**Peak** I^h	**Peak** I^b	**Final** I^h	**Final** I^b
1.0000	30.0000	15.5842	14.6844	15.5842
0.5000	30.0000	15.8818	15.6007	15.8818
0.2000	30.0000	16.3322	16.9624	16.3322
0.1000	30.0000	16.6882	18.0833	16.6882
0.0500	30.0000	17.0473	19.2714	17.0473
0.0200	30.0000	17.5202	20.9375	17.5202
0.0100	30.0000	17.8737	22.2675	17.8737

TABLE 8. Summary of the experimental order of convergence (EOC) for different error norms.

Error Norm	**Mean EOC**	**Std EOC**	**Theoretical order**
L_1 Error	0.2411	0.1168	$\mathcal{O}(\Delta t)^{1.77}$
L_2 Error	0.2411	0.1168	$\mathcal{O}(\Delta t)^{1.77}$
L_∞ Error	0.2411	0.1168	$\mathcal{O}(\Delta t)^{1.77}$

by varying the fractal dimension and fractional-order. The assumed initial conditions are

$$S^{\hbar}(0) = 50, V^{\hbar}(0) = 30, I^{\hbar}(0) = 20, R^{\hbar}(0) = 10,$$
$$S^{b}(0) = 10, V^{b}(0) = 5, I^{b}(0) = 3, R^{b}(0) = 2.$$

The parameter values used in simulation are listed in Table (4) as studied in [27].

Figure 12 displays the human susceptible population at various fractional-orders and fractal dimensions using 2D contour and 3D bar plots. The plots show that higher fractional-orders and higher fractal dimension result in a decreased susceptible population, which means the disease progresses more rapidly. However, lower values of ρ and ζ have higher susceptible populations because they have greater memory and fractal dynamics, which promote a slower spread of disease. The gradient from light to dark colour shows that both fractal-fractional parameters have a combined effect on human susceptibility. This behavior underlines the better performance of the fractal-fractional model than the classical integer-order models because integer-order models do not describe the memory-type depletion of susceptible individuals. Figure 13 presents the behaviour of the vaccinated human population at various fractional-orders and fractal dimensions. The plot indicates that moderate fractional-orders and large fractal dimensions yield maximum vaccinated populations. This is the balance of efficacy and high memory effects. The fractal-fractional framework shows that the memory effect is moderate; that is, lower ρ delays vaccination uptake, but higher ρ approaches the classical behavior, which has the maximum effect of vaccination programs. The plots reflect that the non-uniform distribution proves the superiority of the fractal-fractional approach over the integer-order models, which would predict a monotonic relationship. From a policy perspective, vaccine strategies should consider the memory-dependent dynamics of the fractal-fractional model. The evolution of infected humans using 3D bar plot and 2D contour plot at five time points and various fractional-orders and fractal dimension is described in Figure 14. The plots show that as the fractional-order approaches unity, so does the fractal dimension ζ, and the infection increases until it becomes the classic integer-order case. On the other hand, lower ρ and lower ζ drastically lower the infection levels because the larger memory effects and fractal dynamics slow the transmission down. The gradient shows the protective effect of fractal-fractional dynamics. This behavior validates the ability of the fractal-fractional model to better describe the memory-dependent behavior of the disease transmission process than the integer-order models, which assume a homogeneous infection level. Figure 15 presents the impact of fractional-order and fractal dimension at various values of time. The recovered humans increase with rising fractional-order and fractal dimension. By declining the values of ρ and ζ, the recovered humans decline due to their delayed dynamics. The contour color is continuous from low recovery to high recovery, which is indicative of the cumulative effect of memory in the recovery patterns of the model. This behaviour confirms that the fractal-fractional approach is superior to the integer-order models in describing the temporal evolution of immunity, as the recovery time delays are determined by previous infections. Figure 16 provides the influence of varying time at numerous fractional-orders and fractal dimensions on susceptible birds. The plots show that higher fractional-orders and fractal dimensions result in lower susceptibility to birds, meaning a faster spreading rate of the disease in the bird population. Both lower ρ and ζ lead to the more persistent presence of susceptible populations, which is the delayed dynamics that the fractal-fractional model captures. Due to their high turnover rates and short life spans, birds exhibit the pattern more clearly than humans. This behavior is evidence of the difficulty of capturing species-specific dynamics within integer-order models and the superiority of the fractal-fractional model. Figure 17 shows the impact of fractional-order and fractal dimension

on the vaccinated birds. The plot reveals that intermediate fractional-order (ρ) and higher fractal dimension (ζ) result in maximum vaccination coverage in birds. This is similar to the human vaccination contour, but has different strength, due to the differences between the human vaccination programs and population dynamics. Unlike integer-order models, which make the assumption of an instantaneous vaccination response, the fractal-fractional model shows that a vaccination strategy in birds should incorporate the memory effects and fractal dynamics. Figure 18 illustrates the influence of fractal dimension and fractional-order with the passage of time. Increasing the fractional-order and fractal dimension gives much higher bird infection levels. The infection levels are significantly decreased by lower ρ and ζ with a stronger memory effect. The contour has a steep gradient from blue to red, highlighting the strong effect of fractal-fractional parameters on the bird dynamics of disease. This behavior validates the superiority of the fractal-fractional model in describing the dynamics of spread of avian influenza, where memory is a key factor in predicting the occurrence of spillover events. Figure 19 provides the influence of fractional-order and fractal dimension on the recovered birds through the 2D contour plot and 3D bar plot. Increasing the fractional-order and fractal dimension leads to a rise in recovery. Lowering the fractional-order ρ and fractal dimension ζ lowers the recovery. The plot reflects a gradient from low to high recovery, highlighting the temporal characteristics of recovery in bird populations. Such behavior is an indication of the superiority of the fractal-fractional approach to represent the ecological dynamics of avian influenza, in which the memory effects and fractal behavior are very significant for accurate predictions.

The contour and 3D bar analyses show that the fractal-fractional model is a more biologically realistic model to explain the dynamics of avian influenza than the classical integer-order models. The fractional-order (ρ) and fractal dimension (ζ) make the model much more flexible and capable of modeling memory effects and fractal dynamics, critical for understanding and predicting the spread of disease and the optimal intervention strategies. The robustness and superiority of the fractal-fractional approach are confirmed by the regularity observed in all compartments. We find that the sensitivity to fractional-order implies that the history of exposure is important to the current dynamics of outbreaks. The lagged peaks at lower values of ρ suggest that windows of opportunity for interventions may be longer for populations with high memory effects. The meeting at higher ρ indicates that classical models could be suitable for outbreak dynamics in rapidly changing populations. The fractional-order reflects the hereditary and memory characteristics of the disease system, in which immunity, environmental contamination, and changes in population exhibit time-dependent properties. The differences in dynamics between values of ρ illustrate the need to consider memory effects when making long-term predictions and control strategies for outbreaks.

The numerical values of all compartments at different times are given below for different fractional-order ρ and fractal dimension ζ. These tables offer quantitative evidence of system dynamics and their effect on disease progression in terms of fractal-fractional parameters. Table 9 presents the temporal evolution of all compartments at fixed fractal dimension $\zeta = 0.7$ with different fractional-orders. The table shows that a higher rate ρ slows down the onset of the disease, resulting in a longer time period of susceptible individuals. Table 10 shows the values of the compartments at fractal dimension $\zeta = 0.8$. The intermediate fractal dimension indicates a transition in dynamics as the memory effects start to become

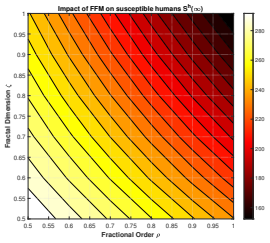

(A) Impact of fractional-order and fractal dimension on susceptible humans through a 2D contour plot.

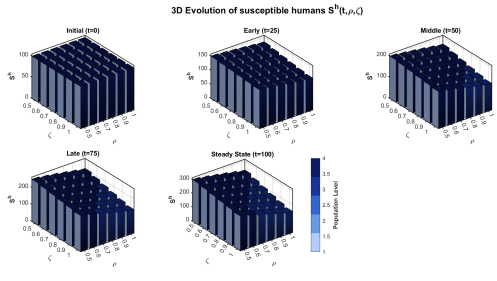

(B) 3D bar plot showing the impact of fractional-order and fractal dimension on susceptible humans at five time points.

FIGURE 12. Behaviour of susceptible humans under the fractal fractional operator with Mittag-Leffler memory through 2D contour and 3D bar plots.

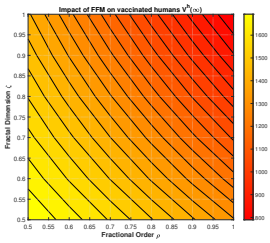

(A) Impact of fractional-order and fractal dimension on vaccinated humans through the 2D contour plot.

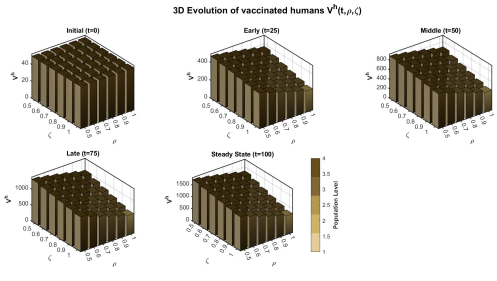

(B) 3D bar plot showing the impact of fractional-order and fractal dimension on vaccinated humans at five time points.

FIGURE 13. Behaviour of vaccinated humans under the fractal-fractional operator with Mittag-Leffler memory through the 2D contour and 3D bar plots.

weaker at $\zeta = 0.7$ and the disease spreads more quickly. Table 11 indicates the dynamics of the system for a fractal dimension of $\zeta = 0.9$. The system looks more like classical behavior at this higher fractal dimension, with the susceptible becoming depleted faster and the peaks of infection occurring earlier. The classical case, corresponding to $\zeta = 1.0$, is shown in Table 12. This is the reference point for the comparison analysis of the effects of fractal-fractional dynamics. Table 13 compares the effect of all four fractal dimensions only for infected humans and birds at the fractional-order $\rho = 0.8$. The sensitivity of the infection dynamics to the fractal dimension is highlighted in this table. For combinations of ρ and ζ, the steady-state values of all compartments are summarized in Table 14. The table

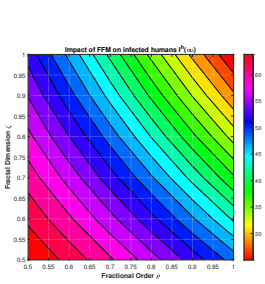

(A) Impact of fractional-order and fractal dimension on infected humans through the 2D contour plot.

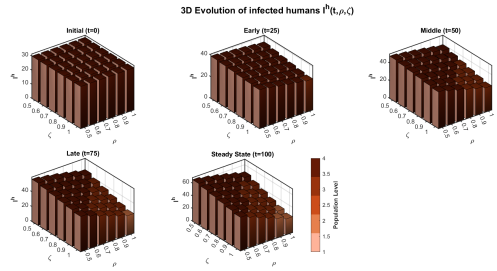

(B) 3D bar plot showing the impact of fractional-order and fractal dimension on infected humans at five time points.

FIGURE 14. Behaviour of infected humans under the fractal fractional operator with Mittag-Leffler memory through 2D contour and 3D bar plots.

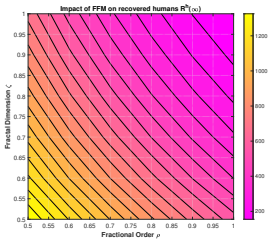

(A) Impact of fractional-order and fractal dimension on recovered humans through the 2D contour plot.

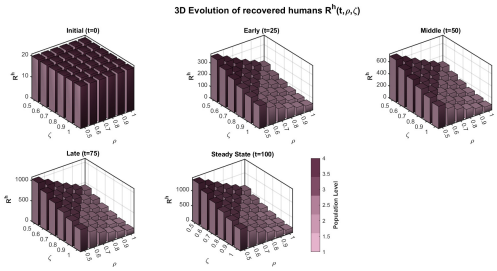

(B) 3D bar plot showing the impact of fractional-order and fractal dimension on recovered humans at five time points.

FIGURE 15. Behaviour of recovered humans under the fractal-fractional operator with Mittag-Leffler memory through 2D contour and 3D bar plots.

shows how the equilibrium values vary with the fractional-order and the fractal dimension. These tables indicate that small fractional-order and the fractal dimension have protective effects, which result in a lesser speed of disease transmission, whereas higher values are closer to classical behavior with disease transmission increasing. The tables demonstrate the ability of the fractal-fractional framework to represent memory-dependent dynamics, which the integer-order models cannot represent.

Due to its capacity to encode both spatial heterogeneity via the fractal dimension ζ and memory effects through the fractional-order ρ, the FFM derivative significantly improves the ability of the Avian Influenza model to capture realistic epidemic dynamics. By offering

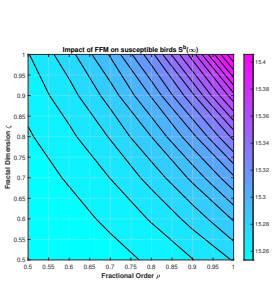

(A) Impact of fractional-order and fractal dimension on susceptible birds through the 2D contour plot.

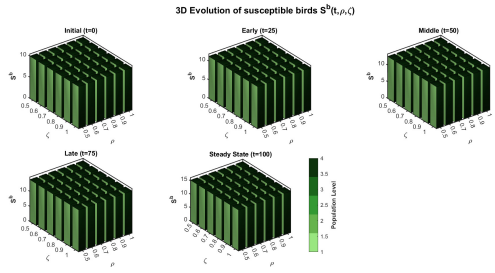

(B) 3D bar plot showing the impact of fractional-order and fractal dimension on susceptible birds at five time points.

FIGURE 16. Behaviour of susceptible birds under the fractal fractional operator with Mittag-Leffler memory through 2D contour and 3D bar plots.

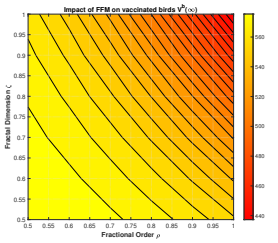

(A) Impact of fractional-order and fractal dimension on vaccinated birds through the 2D contour plot.

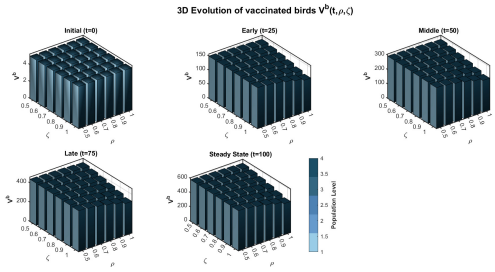

(B) 3D bar plot showing the impact of fractional-order and fractal dimension on vaccinated birds at five time points.

FIGURE 17. Behaviour of vaccinated birds under the fractal fractional operator with Mittag-Leffler memory through the 2D contour and 3D bar plots.

more accurate immunity loss, varied transmission patterns, and more precise time dynamics, the comparison study overall validates that the FFM framework surpasses integer-order models. For simulating the complex dynamics of Avian Influenza in both humans and birds, the FFM approach provides a mathematically flexible and biologically richer way by naturally mixing memory kernels and fractal scaling. By more precisely predicting epidemic peaks and describing vaccination efficacy as a time-dependent process, the FFM model increases accuracy and captures the progressive loss of immunity. Spatial accuracy is further improved by adding a fractal dimension, which captures regional grouping and heterogeneous mixing. Biologically, using hereditary kernels results in memory effects, which produce gradual declines, delayed spikes, and smoother epidemic curves that better

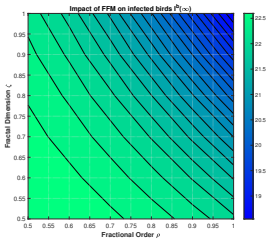

(A) Impact of fractional-order and fractal dimension on infected birds through the 2D contour plot.

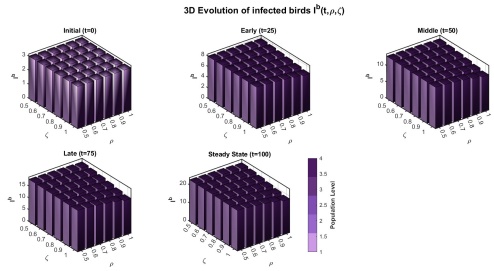

(B) 3D bar plot showing the impact of fractional-order and fractal dimension on infected birds at five time points.

FIGURE 18. Behaviour of infected birds under the fractal fractional operator with Mittag-Leffler memory through 2D contour and 3D bar plots.

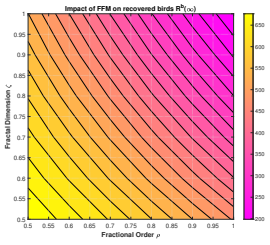

(A) Impact of fractional-order and fractal dimension on susceptible humans through the 2D contour plot.

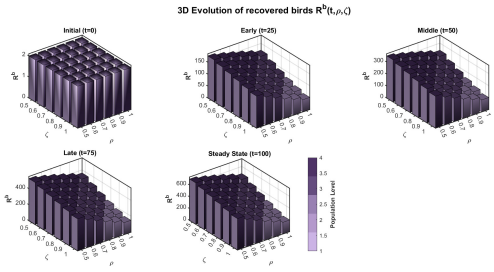

(B) 3D bar plot showing the impact of fractional-order and fractal dimension on recovered birds at five time points.

FIGURE 19. Behavior of recovered birds under the fractal fractional operator with Mittag-Leffler memory through 2D contour and 3D bar plots.

represent immune response and exposure. By integrating long-term memory, geographic complexity, and realistic waning immunity, the FFM operator enhances Avian Influenza modeling overall and offers greater biological relevance and accurate forecasting.

Figure 20 presents the summary of contributions and outcomes of the study.

8. CONCLUSION

8.1. **Summary.** In this study, we have proposed a novel fractal-fractional Avian Influenza model in the Mittag-Leffler sense in order to highlight the effects of vaccination on infected humans and birds. We have performed comprehensive qualitative and quantitative analysis including the existence of a positive and bounded solution, the influenza-free and existing equilibrium points, the threshold parameter $\mathcal{R}_0$, the stability of the influenza-free

TABLE 9. All compartments at fractal dimension $\zeta = 0.7$ for different fractional-orders.

Time	Human compartments				Bird compartments			
	S^h	V^h	I^h	R^h	S^b	V^b	I^b	R^b
Fractional-order $\rho = 0.6$								
0	100.00	50.00	30.00	20.00	10.00	5.00	3.00	2.00
25	129.07	638.86	18.35	102.62	15.51	379.53	16.79	132.27
50	191.28	1043.01	36.46	296.26	15.32	508.42	20.65	323.46
75	237.04	1339.80	49.56	592.20	15.28	556.66	22.06	484.31
100	271.52	1562.41	58.83	957.57	15.26	575.10	22.59	607.47
Fractional-order $\rho = 0.7$								
0	100.00	50.00	30.00	20.00	10.00	5.00	3.00	2.00
25	120.28	581.83	15.83	88.42	15.58	353.54	15.95	109.43
50	177.97	956.51	32.55	238.60	15.35	487.72	20.04	279.10
75	221.87	1241.58	45.30	474.83	15.29	544.09	21.69	430.06
100	255.95	1461.98	54.71	773.25	15.27	568.27	22.39	552.13
Fractional-order $\rho = 0.8$								
0	100.00	50.00	30.00	20.00	10.00	5.00	3.00	2.00
25	111.84	527.02	13.41	77.14	15.68	326.32	15.02	88.77
50	164.70	870.28	28.65	190.97	15.38	463.60	19.33	236.54
75	206.29	1140.49	40.82	375.29	15.30	527.71	21.22	375.12
100	239.50	1355.67	50.23	613.65	15.27	558.34	22.11	493.09
Fractional-order $\rho = 0.9$								
0	100.00	50.00	30.00	20.00	10.00	5.00	3.00	2.00
25	103.87	475.21	11.17	68.49	15.83	298.35	13.96	70.60
50	151.74	786.06	24.87	152.78	15.41	436.37	18.52	196.82
75	190.60	1038.63	36.25	293.38	15.33	507.24	20.62	321.22
100	222.50	1245.61	45.47	479.46	15.29	544.57	21.71	432.26
Fractional-order $\rho = 1.0$								
0	100.00	50.00	30.00	20.00	10.00	5.00	3.00	2.00
25	96.48	426.99	9.20	62.03	16.06	270.04	12.75	55.14
50	139.32	705.36	21.27	122.99	15.46	406.57	17.62	160.70
75	175.14	938.10	31.71	227.88	15.35	482.67	19.89	269.93
100	205.31	1134.10	40.53	369.83	15.31	526.45	21.18	371.71

equilibrium points, the existence of forward transcritical bifurcation, and the identification of sensitive parameters through local and global sensitivity analysis. We have provided statistical analysis to show the symmetric behavior of the model. In order to obtain numerical solutions with various fractional-orders at different fractal dimensions, we have constructed a numerical procedure based on Newton polynomials. The numerical simulations performed through 2D contour plots and 3D bar plots at five time points, various

TABLE 10. All compartments at fractal dimension $\zeta = 0.8$ for different fractional-orders.

Time	Human compartments				Bird compartments			
	S^h	V^h	I^h	R^h	S^b	V^b	I^b	R^b
Fractional-order $\rho = 0.6$								
0	100.00	50.00	30.00	20.00	10.00	5.00	3.00	2.00
25	122.43	595.81	16.44	91.66	15.56	360.12	16.17	114.91
50	181.28	978.02	33.52	251.96	15.34	493.18	20.20	289.98
75	225.69	1266.30	46.38	502.30	15.28	547.55	21.79	443.65
100	259.91	1487.52	55.77	816.74	15.26	570.23	22.45	566.27
Fractional-order $\rho = 0.7$								
0	100.00	50.00	30.00	20.00	10.00	5.00	3.00	2.00
25	113.29	536.46	13.83	78.93	15.66	331.18	15.19	92.23
50	167.02	885.36	29.33	198.64	15.37	468.08	19.46	243.85
75	209.05	1158.39	41.62	391.51	15.30	530.89	21.31	384.76
100	242.44	1374.71	51.04	639.89	15.27	560.34	22.16	503.67
Fractional-order $\rho = 0.8$								
0	100.00	50.00	30.00	20.00	10.00	5.00	3.00	2.00
25	104.71	480.65	11.40	69.31	15.81	301.40	14.08	72.44
50	153.12	795.03	25.27	156.48	15.41	439.45	18.61	200.95
75	192.30	1049.62	36.74	301.42	15.32	509.66	20.69	326.96
100	224.35	1257.63	45.99	492.77	15.29	546.27	21.76	438.87
Fractional-order $\rho = 0.9$								
0	100.00	50.00	30.00	20.00	10.00	5.00	3.00	2.00
25	96.79	429.02	9.28	62.27	16.05	271.29	12.80	55.76
50	139.85	708.81	21.42	124.13	15.46	407.92	17.66	162.21
75	175.81	942.46	31.90	230.44	15.35	483.83	19.93	272.11
100	206.06	1138.99	40.75	374.15	15.30	527.34	21.20	374.33
Fractional-order $\rho = 1.0$								
0	100.00	50.00	30.00	20.00	10.00	5.00	3.00	2.00
25	89.60	381.96	7.63	57.20	16.39	241.30	11.35	42.24
50	127.42	628.11	17.85	100.03	15.53	374.31	16.62	128.14
75	159.92	839.18	27.24	176.14	15.39	453.78	19.04	221.72
100	187.98	1021.57	35.47	281.41	15.33	503.29	20.50	312.40

fractional-orders, and fractal dimensions reveal that the susceptible, vaccinated, and recovered classes observe a slow decline, while infected classes grow slowly as compared to the quicker decrease or increase expected by integer-order models due to the memory effects associated with fractional-order and fractal dimension. Phase plots illustrating the interaction between the human and bird compartments have been provided.

TABLE 11. All compartments at fractal dimension $\zeta = 0.9$ for different fractional-orders.

Time	Human compartments				Bird compartments			
	S^h	V^h	I^h	R^h	S^b	V^b	I^b	R^b
Fractional-order $\rho = 0.6$								
0	100.00	50.00	30.00	20.00	10.00	5.00	3.00	2.00
25	116.25	555.71	14.67	82.76	15.62	340.86	15.53	99.41
50	171.70	915.80	30.71	214.96	15.36	476.79	19.72	258.78
75	214.57	1194.25	43.21	425.76	15.30	536.88	21.48	404.19
100	248.30	1412.57	52.65	695.00	15.27	564.03	22.27	524.70
Fractional-order $\rho = 0.7$								
0	100.00	50.00	30.00	20.00	10.00	5.00	3.00	2.00
25	106.89	494.85	12.01	71.55	15.76	309.22	14.39	77.31
50	156.70	818.29	26.31	166.49	15.40	447.24	18.85	211.79
75	196.66	1077.97	38.02	323.03	15.32	515.65	20.86	341.84
100	229.11	1288.47	47.34	528.36	15.28	550.39	21.88	455.87
Fractional-order $\rho = 0.8$								
0	100.00	50.00	30.00	20.00	10.00	5.00	3.00	2.00
25	98.29	438.79	9.67	63.48	15.99	277.19	13.07	58.78
50	142.39	725.32	22.16	129.78	15.45	414.29	17.86	169.45
75	179.00	963.23	32.84	242.96	15.35	489.24	20.09	282.55
100	209.64	1162.24	41.78	395.28	15.30	531.46	21.32	386.85
Fractional-order $\rho = 0.9$								
0	100.00	50.00	30.00	20.00	10.00	5.00	3.00	2.00
25	90.52	388.00	7.82	57.79	16.34	245.30	11.56	43.87
50	129.03	638.58	18.32	102.85	15.52	378.91	16.77	132.43
75	162.01	852.73	27.85	182.56	15.38	458.04	19.17	228.18
100	190.38	1037.16	36.18	292.47	15.33	506.81	20.60	320.48
Fractional-order $\rho = 1.0$								
0	100.00	50.00	30.00	20.00	10.00	5.00	3.00	2.00
25	83.58	342.67	6.66	53.72	16.77	214.07	9.92	32.41
50	116.80	559.23	14.82	83.72	15.62	342.15	15.57	101.00
75	146.01	748.78	23.19	138.38	15.43	422.89	18.11	179.97
100	171.79	916.31	30.71	215.58	15.36	476.62	19.72	259.14

8.2. **Findings.** The chaos test verifies that the model does not exhibit chaotic oscillations, and the behavior of all compartments is bounded. The two factors that have the most positive impact on $\mathcal{R}_0$ are the bird-to-bird transmission rate χ and the bird recruitment rate ϕ. However, sensitivity indices increases in the bird natural death rate, vaccination rate κ, and recovery rate have significant effects on $\mathcal{R}_0$. Disease-induced mortality has the least impact. The convergence and stability analysis reveals that the Newton polynomial scheme

TABLE 12. All compartments at fractal dimension $\zeta = 1.0$ for different fractional-orders.

Time	Human compartments				Bird compartments			
	S^h	V^h	I^h	R^h	S^b	V^b	I^b	R^b
Fractional-order $\rho = 0.6$								
0	100.00	50.00	30.00	20.00	10.00	5.00	3.00	2.00
25	110.52	518.44	13.03	75.58	15.70	321.85	14.86	85.66
50	162.58	856.52	28.03	184.19	15.38	459.41	19.21	229.92
75	203.76	1124.05	40.09	360.91	15.31	524.69	21.13	366.31
100	236.78	1338.11	49.48	590.28	15.28	556.39	22.05	483.35
Fractional-order $\rho = 0.7$								
0	100.00	50.00	30.00	20.00	10.00	5.00	3.00	2.00
25	101.04	456.76	10.39	65.84	15.90	287.80	13.53	64.50
50	147.03	755.45	23.50	140.73	15.43	425.51	18.19	182.88
75	184.79	1000.83	34.54	267.10	15.34	498.54	20.36	301.69
100	216.08	1204.02	43.64	435.74	15.29	538.34	21.52	409.51
Fractional-order $\rho = 0.8$								
0	100.00	50.00	30.00	20.00	10.00	5.00	3.00	2.00
25	92.52	401.11	8.26	59.13	16.23	253.82	11.98	47.52
50	132.51	661.18	19.31	109.23	15.49	388.58	17.07	141.82
75	166.48	881.84	29.16	197.03	15.37	466.84	19.43	242.21
100	195.50	1070.44	37.68	317.33	15.32	513.99	20.81	337.89
Fractional-order $\rho = 0.9$								
0	100.00	50.00	30.00	20.00	10.00	5.00	3.00	2.00
25	84.97	351.69	6.84	54.47	16.68	220.52	10.26	34.54
50	119.26	575.17	15.52	87.16	15.59	349.90	15.83	107.11
75	149.26	769.88	24.13	146.44	15.42	430.51	18.34	189.50
100	175.60	941.08	31.83	229.75	15.35	483.36	19.92	271.46
Fractional-order $\rho = 1.0$								
0	100.00	50.00	30.00	20.00	10.00	5.00	3.00	2.00
25	78.33	308.52	6.30	51.03	17.17	188.56	8.55	25.09
50	107.41	498.21	12.16	72.26	15.75	310.67	14.44	78.72
75	133.42	667.08	19.57	111.08	15.49	390.89	17.14	144.40
100	156.84	819.18	26.34	167.14	15.40	447.24	18.84	212.33

is reliable and accurate in simulating the fractal-fractional avian influenza model. The scheme shows convergence and is quite stable with all step sizes, which is suitable for long-term epidemiological simulations. The numerical simulations confirm a strong agreement between the mathematical model and numerical results, suggesting that the stability of the equilibrium is not affected by the fractal-fractional derivative. It has been found that raising

TABLE 13. Infection compartments at different time points.

Time	$\zeta = 0.7$		$\zeta = 0.8$		$\zeta = 0.9$		$\zeta = 1.0$	
	I^h	I^b	I^h	I^b	I^h	I^b	I^h	I^b
fractional-order $\rho = 0.8$								
0	30.00	3.00	30.00	3.00	30.00	3.00	30.00	3.00
25	13.41	15.02	11.40	14.08	9.67	13.07	8.26	11.98
50	28.65	19.33	25.27	18.61	22.16	17.86	19.31	17.07
75	40.82	21.22	36.74	20.69	32.84	20.09	29.16	19.43
100	50.23	22.11	45.99	21.76	41.78	21.32	37.68	20.81

TABLE 14. Steady state values of all compartments.

(ρ, ζ)	S^h	V^h	I^h	R^h	S^b	V^b	I^b	R^b
(0.6,0.7)	271.52	1562.41	58.83	957.57	15.26	575.10	22.59	607.47
(0.8,0.7)	239.50	1355.67	50.23	613.65	15.27	558.34	22.11	493.09
(1,0.7)	205.31	1134.10	40.53	369.83	15.31	526.45	21.18	371.71
(0.6,0.8)	259.91	1487.52	55.77	816.74	15.26	570.23	22.45	566.27
(0.8,0.8)	224.35	1257.63	45.99	492.77	15.29	546.27	21.76	438.87
(1,0.8)	187.98	1021.57	35.47	281.41	15.33	503.29	20.50	312.40
(0.6,0.9)	248.30	1412.57	52.65	695.00	15.27	564.03	22.27	524.70
(0.8,0.9)	209.64	1162.24	41.78	395.28	15.30	531.46	21.32	386.85
(1,0.9)	171.79	916.31	30.71	215.58	15.36	476.62	19.72	259.14
(0.6,1)	236.78	1338.11	49.48	590.28	15.28	556.39	22.05	483.35
(0.8,1)	195.50	1070.44	37.68	317.33	15.32	513.99	20.81	337.89
(1,1)	156.84	819.18	26.34	167.14	15.40	447.24	18.84	212.33

the fractal and fractional parameter values causes the solution curves to converge to their respective stable states more quickly.

8.3. **Recommendations for eradication of Influenza.** The analysis provides obvious biological recommendations:

- Reducing $\mathcal{R}_0 < 1$ is necessary for disease elimination, producing an elimination threshold with predictable intervention reactions. The transmission rate $\chi^\star$ provides an accurate quantitative target. In order to preserve $\mathcal{R}_0 < 1$, control techniques must reduce bird-to-bird transmission χ through improved biosecurity.
- The statistically significant effect of vaccination indicates that human vaccination serves as a secondary means of protection when there is not full control of bird infections. Increase κ through immunization programs to maintain stability even at higher transmission rates,
- The negative effect of bird recovery suggests that supportive care and early treatment in the poultry farms will decrease the spread of the infection, because healthy birds will recover faster.

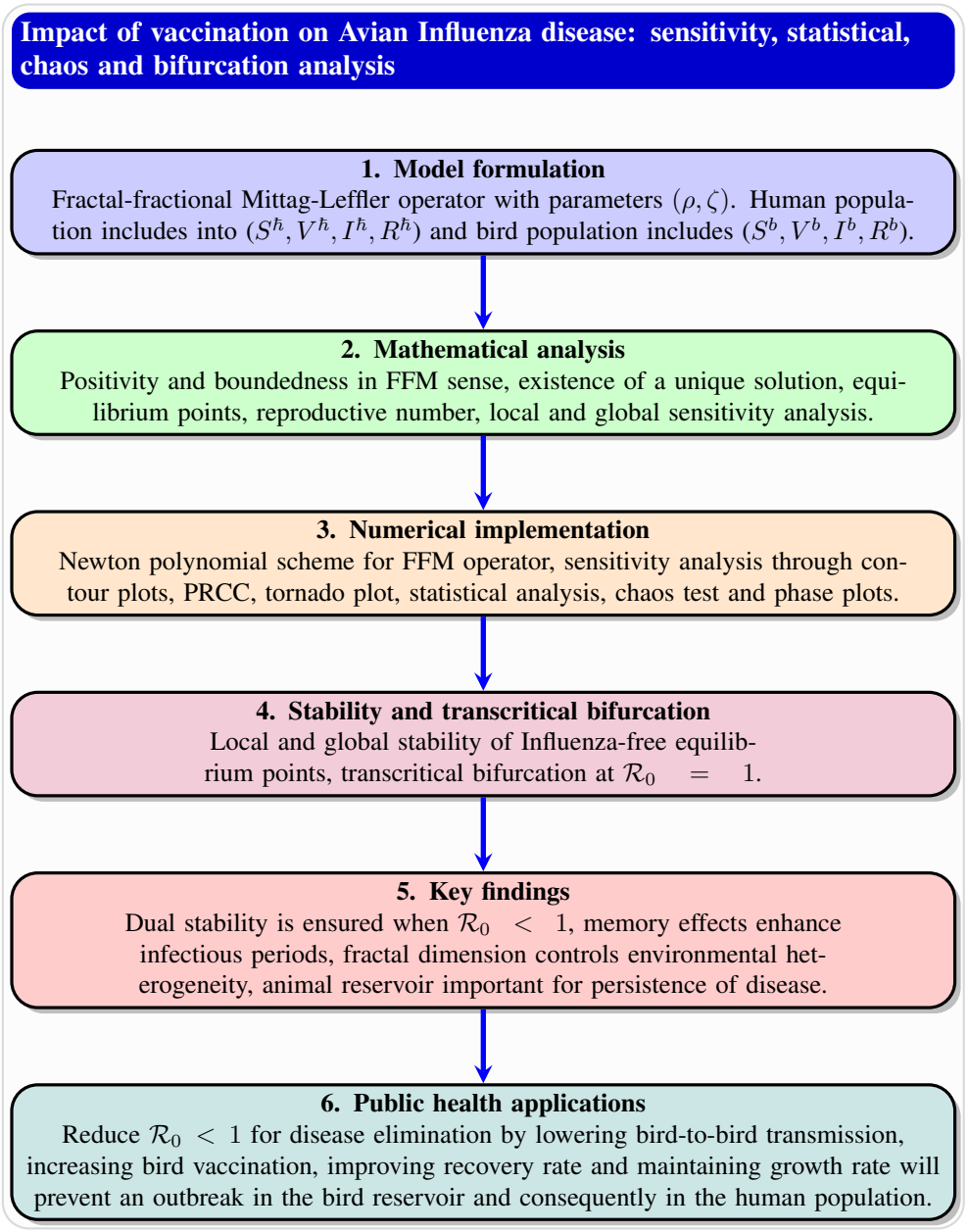

FIGURE 20. Flowchart for the Avian Influenza model with human-birds transmission dynamics.

- Bird recruitment ϕ is a good sign of spreading control, so lower density of poultry and stamping-out precautions can control spread.

- All of the top-ranked parameters are bird-related and highlight the need to focus primary prevention efforts on the reservoir population. This will prevent an outbreak in the bird reservoir and, consequently, in the human population.

Overall, our analysis provides useful insights by highlighting prevention of bird transmission by safety measures and vaccination, predicting outbreak trajectories near crucial parameters, and computing the minimum vaccination requirements for disease-free stability. The bifurcation offers reliable ideas for managing zoonotic overload in the avian influenza environment by filling the gap between epidemiological policy and mathematical accuracy.

8.4. **Limitations and future work.** The suggested model uses some simplifying assumptions, even if it successfully reflects the essential dynamics of avian influenza throughout human and bird populations. The model ignores age-dependent susceptibilities, occupational risk variations, and spatial clustering heterogeneity in the real world by assuming homogeneous mixing. Despite their known role in the spread of avian influenza, environmental transmission pathways such as the virus's ability to remain in water or on contaminated surfaces are not incorporated. The extension of the model to other avian influenza viruses with unique epidemiological characteristics is limited because it is customized to H5N1-specific factors. The possibility that within a season some recovered people become susceptible has not been considered due to the short time span of one season, but this can affect vaccine efficacy. Since there was difficulty accessing experimental data from health authorities, the model analysis and simulations were limited to theoretical data extracted from the literature. This study assumed that the overall population is constant, meaning that birth and natural death rates are balanced and that migration, demographic changes, or infection-induced mortality do not affect population size. However, in reality, various variables can impact population dynamics, such as urbanization, seasonal labor migration, and public health initiatives, all of which may have an impact on disease transmission. The proposed model does not include the novel disease pathogen variations and time-dependent public behavior.

There are multiple ways to build upon the current research. Investigating stochastic and fractional stochastic versions of the proposed model could serve as a promising direction for future studies. Both biological realism and forecasting ability can be improved by future developments. Inter-regional transmission between farms, wetlands, and urban areas would be more accurately represented by incorporating spatial heterogeneity through metapopulation or reaction-diffusion techniques. The ecological correctness of the framework can be improved by explicitly simulating asymptomatic avian carriers and environmental reservoirs. Additionally, the inclusion of time-dependent treatments like vaccination or culling techniques would enhance the model's usability for real-time public health planning, while the introduction of stochasticity or fuzzy formulations could represent outbreak variability in small populations. We can assume that vaccine efficacy varies with age. Another strategy in the future is to develop a mathematical model with vaccinated and unvaccinated populations with different behaviors. Future work should focus on including experimental data when accessible to perform model analysis and simulations in order to inform policymakers about the spread and control of the two diseases.

CREDIT AUTHORSHIP CONTRIBUTION'S STATEMENT

Usama Atta: Investigation; Software; Conceptualization; Methodology. Aqeel Ahmad: Validation; Writing - original draft; Resources; Supervision. Sadia Sattar: Writing - review & editing; Visualization; Resources; Data curation.

DECLARATIONS

Conflict of i nterest. The authors of this paper state that they do not have any conflict of interest. The authors have read and agreed to the published version of the manuscript.

Funding statement. Not applicable.

Acknowledgments. We thank the reviewers for their useful suggestions, which helped a lot to improve this paper.

Data availability statement. The data utilized in the research is available in the manuscript.

REFERENCES

[1] M. A. Abdoon and A. B. Alzahrani. Comparative analysis of influenza modeling using novel fractional operators with real data. *Symmetry*, **16** No.9, (2024) 1126.

[2] M. A. Abdoon, R. Saadeh, M. Berir, and F. E. Guma. Analysis, modeling and simulation of a fractional-order influenza model. *Alexandria Engineering Journal*, **74**, (2023) 231-240.

[3] W. Ahmad, M. A. Nazir, M. Rafiq, A. I. K. Butt, N. Ahmad, and M. Hussain. Analyzing optimal control techniques in a nonlinear fractional Rubella model with the Atangana–Baleanu derivative. *Computers in Biology and Medicine*, **197**, (2025) 110954.

[4] C. Andreu-Vilarroig, G. González-Parra, and R. J. Villanueva. Mathematical Modeling of Influenza Dynamics: Integrating Seasonality and Gradual Waning Immunity. *Bulletin of Mathematical Biology*, **87** No.6, (2025) 75.

[5] M. Al-Qureshi, S. Rashid, F. Jarad, and M. S. Alharthi. Dynamical behavior of a stochastic highly pathogenic avian influenza A (HPAI) epidemic model via piecewise fractional differential technique. *AIMS Mathematics*, **8** No.1, (2023) 1737-1756.

[6] M. Altaf Khan, M. H. DarAssi, I. Ahmad, E. Alzahrani, and N. Mat Isa. Existence, Stability, and Data-Driven Analysis of a Fractional-Order Avian Influenza Model in Poultry Farms. *Engineering Reports*, **8** No.3, (2026) e70711.

[7] S. M. Alzahrani, R. Saadeh, M. A. Abdoon, A. Qazza, F. E. Guma, and M. Berir. Numerical simulation of an influenza epidemic: Prediction with fractional SEIR and the ARIMA model. *journal Applied Mathematics*, **18** No.1, (2024) 1-12.

[8] E. O. Alzahrani and M. A. Khan. Comparison of numerical techniques for the solution of a fractional epidemic model. *The European Physical Journal Plus*, **135** No.1, (2020) 110.

[9] C. Andreu-Vilarroig, R. J. Villanueva, and G. González-Parra. Mathematical modeling for estimating influenza vaccine efficacy: A case study of the Valencian Community, Spain. *Infectious Disease Modelling*, **9** No.3, (2024) 744-762.

[10] A. Atangana. Fractal-fractional differentiation and integration: connecting fractal calculus and fractional calculus to predict complex system. *Chaos, Solitons and Fractals*, **102**, (2017) 396-406.

[11] A. Atangana and D. Baleanu. New fractional derivatives with nonlocal and non-singular kernel: theory and application to heat transfer model. *arXiv preprint arXiv:1602.03408*, (2016).

[12] A. Atangana and S. I. Araz. *New numerical scheme with Newton polynomial: theory, methods, and applications*. Academic Press, (2021).

[13] A. I. K. Butt, W. Ahmad, M. Rafiq, N. Ahmad, and M. Imran. Optimally analyzed fractional Coronavirus model with Atangana–Baleanu derivative. *Results in Physics*, **53**, (2023) 106929.

[14] A. I. K. Butt, W. Ahmad, H. G. Rabbani, M. Rafiq, S. Ahmad, N. Ahmad, and S. Malik. Exploring optimal control strategies in a nonlinear fractional bi-susceptible model for Covid-19 dynamics using Atangana-Baleanu derivative. *Scientific Reports*, **14** No.1, (2024) 31617.

[15] M. Caputo and M. Fabrizio. A new definition of fractional derivative without singular kernel. *Progress in Fractional Differentiation & Applications*, **1** No.2, (2015) 73-85.

[16] C. Castillo-Chavez, C. Kribs, and B. Morin. Student-driven research at the mathematical and theoretical biology institute. *The American Mathematical Monthly*, **124** No.9, (2017) 876-892.

[17] A. Ebrahimzadeh. Fractional optimal control of avian-human influenza with environmental and behavioral interactions. *International Journal of Dynamics and Control*, **14** No. 3, (2026) 101.

[18] European Centre for Disease Prevention and Control. Surveillance systems overview for 2023. Available from: https://www.cdc.gov/bird-flu/situation-summary/index.html

[19] F. Evirgen, E. Uçar, S. Uçar, and N. Ozdemir. Modelling Influenza A disease dynamics under Caputo-Fabrizio fractional derivative with distinct contact rates. *Mathematical Modelling and Numerical Simulation with Applications*, **3** No.1, (2023) 58-73.

[20] H. J. Hamad, S. H. Khoshnaw, and M. Shahzad. Model analysis for an HIV infectious disease using elasticity and sensitivity techniques. *AIMS Bioengineering*, **11** No.3, (2024) 281-300.

[21] A. Hanif, A. I. Kashif Butt, and W. Ahmad. Numerical approach to solve Caputo-Fabrizio-fractional model of corona pandemic with optimal control design and analysis. *Mathematical Methods in the Applied Sciences*, **46** No.8, (2023) 9751-9782.

[22] S. Jamil, P. A. Naik, M. Farman, M. U. Saleem, and A. H. Ganie. Stability and complex dynamical analysis of COVID-19 epidemic model with non-singular kernel of Mittag-Leffler law. *Journal of Applied Mathematics and Computing*, **70** No.4, (2024) 3441-3476.

[23] T. Kanwal, A. Hussain, I. Avcı, S. Etemad, S. Rezapour, and D. F. Torres. Dynamics of a model of polluted lakes via fractal–fractional operators with two different numerical algorithms. *Chaos, Solitons & Fractals*, **181**, (2024) 114653.

[24] A. Khan, G. Ali, A. Khaliq and G. Zaman. Mathematical modeling and dynamical aspects of the co-infection of Buruli ulcer and cholera. *Punjab Univ.j.Math.*, **56** No.8, (2024) 414-445.

[25] H. Khan, A. H. Rajpar, J. Alzabut, M. Aslam, S. Etemad, and S. Rezapour. On a fractal–fractional-based modeling for influenza and its analytical results. *Qualitative Theory of Dynamical Systems*, **23** No.2, (2024) 70.

[26] M. Khan, N. Khan, I. Ullah, K. Shah, T. Abdeljawad, and B. Abdalla. A novel fractal fractional mathematical model for HIV/AIDS transmission stability and sensitivity with numerical analysis. *Scientific Reports*, **15** No.1, (2025) 9291.

[27] M. Kharis and Amidi. Mathematical modeling of Avian Influenza epidemic with bird vaccination in constant population. In *Journal of Physics: Conference Series*, **983** No.1, (2018) 012116.

[28] A. R. Kimbir, T. Aboiyar, and P. N. Okolo. A model analysis for the transmission dynamics of avian influenza. *Mathematical Theory and Modeling*, **4** No.13, (2014) 15-28.

[29] K. A. Kumar and A. Venkatesh. Mathematical analysis of SEITR model for influenza dynamics. *Journal of Computational Analysis and Applications*, **31** No.1, (2023) 281-293.

[30] A. Malek and A. Hoque. A Mathematical Model of Avian Influenza for Poultry Farm and its Stability Analysis. *Applications and Applied Mathematics: An International Journal (AAM)*, **15** No.2, (2020).

[31] A. Malek and A. Hoque. Mathematical modeling of the infectious spread and outbreak dynamics of avian influenza with seasonality transmission for chicken farms. *Comparative Immunology, Microbiology and Infectious Diseases*, **104**, (2024) 102108.

[32] K. S. Nisar, M. Farman, E. Hincal, A. Hasan, and P. Abbas. Chlamydia infection with vaccination asymptotic for qualitative and chaotic analysis using the generalized fractal fractional operator. *Scientific Reports*, **14** No.1, (2024) 25938.

[33] E. Nwagrabe. Mathematical modeling of avian influenza with vaccination and treatment for poultry farms. *International Journal of Functional Research in Science and Engineering (IJFRSE)*, **3** No.2, (2024).

[34] I. C. Nwokike, C. Nwutara, M. O. Ezekoye, K. M. Koko, T. W. Owolabi, G. O. Onukwube, and N. C. Umelo-Ibemere. Fractional-Order Modeling of Within-Host Swine Influenza (H1N1) Dynamics with Autophagy and Immune Response. *Journal of Disease and Global Health*, **19** No.1, (2026) 365-380.

[35] U. Oseni, T. Tivde, K. O. Achema, and R. I. Gweryina. A Mathematical Model for Transmission Dynamics of an Avian Influenza Disease in a Human Population. *Annals of Communications in Mathematics*, **7** No.4, (2024) 328-353.

[36] M. Ozair and H. Alzubadi. Mathematical study of plant disease model using Atangana-Baleanu fractional operators with Beddington-DeAngelis incidence. *Punjab Univ. j.Math.*, **56** No.9, (2024) 505-524.

[37] A. Pandey and S. Ghosh. Dynamical analysis of a fractional-order influenza model with stability and control perspectives. *Engineering Computations*, **43** No.3, (2026) 1183-1218.

[38] M. A. Qureshi, M. A. Samad, and Z. F. Muqadas. An Overview of Avian Flu. *Biological Times*, **1** No.1, (2022) 3.

[39] S. Rit, S. Majee, S. Barman, A. De, and S. Jana. Implementation of Caputo type fractional-order differential equations to investigate the impact of birds-flu incorporating genetic algorithm-based optimization. *The Journal of Analysis*, (2026) 1-22.

[40] W. Sudsutad, C. Thaiprayoon, J. Kongson, and W. Sae-dan. A mathematical model for fractal-fractional monkeypox disease and its application to real data. *AIMS Mathematics*, **9** No.4, (2024) 8516-8563.

[41] F. A. Wireko, I. K. Adu, K. A. Gyamfi, and J. K. K. Asamoah. Modelling the transmission behavior of Measles disease considering contaminated environment through a fractal-fractional Mittag-Leffler kernel. *Physica Scripta*, **99** No.7, (2024) 075025.

[42] World Health Organization. Considerations for use of avian influenza A (H5) vaccines during the inter-pandemic and emergence periods: report of a WHO virtual scientific consultation, September 2024. *World Health Organization*, (2025).

[43] Z. Yaagoub and S. Ahmad. Three-strain epidemic model for influenza virus involving fractional derivative and treatment. *Journal of Applied Mathematics & Computing*, **71** No.1, (2025) 1247-1266.

[44] R. Zarin, U. W. Humphires, H. A. E. W. Khalifa, and A. A. Raezah. Sensitivity analysis and numerical modeling of influenza propagation and intervention strategies under the fractal-fractional operator. *Fractals*, **34** No. 4, (2026) 2540058.

[45] R. Zarin. Artificial neural network-based approach for simulating influenza dynamics: A nonlinear SVEIR model with spatial diffusion. *Engineering Analysis with Boundary Elements*, **176**, (2026) 106230.